ORNL/TM-2016/40

Neutron Scattering of Residual Hydrogen in 1,4-Dioxane-d_8 Liquid: Understanding Measurements with Molecular Dynamics Simulations

Valmor F. de Almeida
Hongjun Liu
Kenneth W. Herwig
Michelle K. Kidder

25 January 2016

OAK RIDGE NATIONAL LABORATORY
MANAGED BY UT-BATTELLE FOR THE US DEPARTMENT OF ENERGY

ORNL/TM-2016/40

Chemical Sciences Division

Neutron Scattering of Residual Hydrogen in 1,4-Dioxane-d_8 Liquid: Understanding Measurements with Molecular Dynamics Simulations

Valmor F. de Almeida, Hongjun Liu, Kenneth W. Herwig, and Michelle K. Kidder

25 January 2016

Prepared by
OAK RIDGE NATIONAL LABORATORY
Oak Ridge, TN 37831-6283
managed by
UT-BATTELLE, LLC
for the
US DEPARTMENT OF ENERGY
under contract DE-AC05-00OR2272

Neutron Scattering of Residual Hydrogen in 1,4-Dioxane-d_8 Liquid: Understanding Measurements with Molecular Dynamics Simulations*

Valmor F. de Almeida, Hongjun Liu‡,
Kenneth W. Herwig† and Michelle K. Kidder

Chemical Sciences Division
Oak Ridge National Laboratory
Oak Ridge, TN 37831-6119, USA

Technical Report ORNL/TM-2016/40

25 January 2016

†Neutron Sciences Directorate, Spallation Neutron Source.
‡Current address: University of Tennessee, Knoxville; Dept. of Chemical and Biomolecular Engineering.
*Also available by request to dealmeidav@ornl.gov

Abstract

That incoherent scattering from protiated molecular liquids adds a constant background to the measured scattering intensity is well known, but less appreciated is the fact that coherent scattering is also induced by the presence of hydrogen in a deuterated liquid. In fact, the scattering intensity can be very sensitive, in the small-q region, with respect to the amounts and distribution of residual H in the system. We used 1,4-dioxane liquid to demonstrate that the partial structure factors of the HD and DD atom pairs contribute significantly to inter-molecular scattering and that uncertainty in the extent of deuteration account for discrepancies between simulations and measurements. Both contributions to uncertainty have similar magnitudes: scattering interference of the hydrogen-deuterium pair, and complementary interference from the deuterium-deuterium pair by virtue of chemical inhomogeneity. This situation arises in practice since deuteration of liquids is often 99 % or less. A combined experimental and extensive computational study of static thermal neutron scattering of 1,4-dioxane demonstrates the foregoing. We show, through simulations, that the reason for the differences is the content of protiated dioxane (vendors quote 1 %). We estimate that up to 5 % (at 298 K and at 343 K) protiated mole fraction may be involved in generating the scattering differences. Finally, we find that the particular distribution of hydrogen in the protiated molecules affects the results significantly; here we considered molecules to be either fully protiated or fully deuterated. This scenario best reconciles the computational and experimental results, and leads us to speculate that the deuteration synthesis process tends to leave a molecule either fully deuterated or fully protiated. Although we have used 1,4-dioxane as a model liquid, the effects described in this study extend to similar liquids and similar systematic experimental/computational studies can be performed to either understand measurements or calibrate/validate molecular dynamics models.

Contents

List of Figures

List of Tables

1 Introduction

Elastic neutron scattering of 1,4-dioxane, a common cyclic diether solvent, is used here as a model for a combined neutron scattering/molecular dynamics simulation study. Although one previous neutron scattering study investigated the liquid structure of dioxane (Bako *et al.*, 1999), it did not apply molecular dynamics simulations (MD) to extend the insight obtained from experiments nor did it study the low-momentum transfer range. Therefore one aspect of this work was to extend the study of dioxane to a unexplored domain, and another aspect was to use MD simulations as a complementary tool to neutron scattering measurements in order to extract molecular structure information from collected data (Benmore and Loh, 2000). We provide here a detailed account of the analysis of new small-angle neutron scattering data, and existing wide-angle data for dioxane through the computation of static, partial structure factors. We explain the origin of coherent scattering in the small-angle scattering range, we validate various aspects of the MD model based on the short-range structure of dioxane, and we identify shortcomings of scattering data reduction in the presence of unavoidable inelastic scattering effects in the instrument. This report demonstrates that neutron scattering measurements and simulation predictions support each other to improve our understanding of the problem, and we hope we provide a realistic description of the effort needed to obtain the level of understanding desired.

In order to explore combined scattering and molecular dynamics simulations, an all-atom force field must be employed since any united-atom approach (Geerlings *et al.*, 2000; Krienke *et al.*, 2004; Nagy *et al.*, 2008) will lack the needed hydrogen/deuterium information. The all-atom force field used in this study has been proposed and tested by comparison of results against thermodynamic, structural and dynamical properties (Cinacchi *et al.*, 2006). We use this force field without modifications in conjunction with the MD code LAMMPS (Plimpton, 1995).

The computational work focuses on computing partial structure factors and relating them, rigorously, to the central quantity measured in static neutron scattering experiments, namely, the differential scattering cross section. Despite the longevity of scattering theory, the connections with MD simulations and experimental measurements is not easily accessible. Therefore an additional contribution of this report is to collect in one place the formulae, their underlying assumptions, and corresponding modern computational procedures needed for understanding the experimental and simulation results. Some disagreements between results found in the course of this work would not have been resolved if the quantities measured (including those in data reduction) and quantities obtained from simulations were not rigorously related by theory.

2 Elements of polyatomic scattering theory

Thermal neutron scattering provides structural information of molecular liquids. Measurements can be compared against classical atomistic simulations and help improve the underlying theory and modeling approach, in particular, to gain confidence on the force field potentials employed. Conversely, a credible molecular model helps gain unique insight on quantities inaccessible to measurements, thereby extending the value of experimental work. For polyatomic systems, structural information is contained in the partial structural factors which require additional experimental information. We collect in this section elements of the theory of partial structure factors as applied to liquids.

The central quantity directly measured by elastic neutron scattering instruments is the differential scattering cross section of the sample system, $\frac{d\sigma}{d\Omega}$, defined as the ratio of scattered neutrons per unit of solid angle to the incident neutron flux, about a given scattering direction $\hat{\boldsymbol{s}}$ ($\left\|\hat{\boldsymbol{s}}\right\| = 1$), that is,

$$\frac{d\sigma}{d\Omega}(\hat{\boldsymbol{s}}) := \frac{J(\hat{\boldsymbol{s}})}{J_0} \ , \tag{2.1}$$

where J is measured in units of number of scattered neutrons per solid angle per time, and J_0 is measured in units of number of incident neutrons per area normal to the incident beam per time. This gives $\frac{d\sigma}{d\Omega}$ the unit of area per solid angle; typically $\mathrm{b\,sr^{-1}}$ (b stands for 1 barn=100 $\mathrm{fm^2}$).

The spatial direction dependence of (2.1) is related to the molecular structure of the fluid. In experiments, a known volume of fluid is exposed to a collimated beam of neutrons which approximates a plane wave. The flux ratio (2.1) is then approximately measured (depending on various instrument parameters) per unit of volume of the sample, and denoted

$$\frac{d\Sigma}{d\Omega}(\hat{\boldsymbol{s}}) \approx V^{-1}\frac{J(\hat{\boldsymbol{s}})}{J_0} \ . \tag{2.2}$$

This experimental quantity, the macroscopic differential scattering cross section, is an average over the irradiated volume of the sample for a given finite distribution of detectors positioned around and far from the sample. When the flux ratio is actually measured, as opposed to just counting the number of scattered neutrons in J alone, the experimental value of $\frac{d\Sigma}{d\Omega}$ is said to be in *absolute* units, which typically means in units of $\mathrm{cm^{-1}}$. The actual formula used in the approximation (2.2) depends on the various elements of the particular diffractometer used. In this work we utilized the EQ-SANS instrument in the Oak Ridge National Laboratory Spallation Neutron Source which has online and published information (Zhao, 2000, 2001; Zhao *et al.*, 2010).

A central purpose of scattering theory is to calculate J from the interaction of neutrons with the sample system composed of a constellation of atoms. Specifically this entails a scattering collision quantum mechanical problem of neutrons and nuclei via the long-range portion of strong forces and it is not a simple undertaking except for the most elementary scattering systems (SQUIRES, 1996). Nevertheless under some rather restrictive assumptions met in practice, namely, single scattering event between incident neutron and nucleon; weak scattering so that the same incident neutron flux falls on all nuclei (negligible attenuation); long distance between the scattering center and detection of the scattered neutron so to make the subtended solid angle at the sample be well defined; length scale of the scattering object (atomic nuclei) much smaller than the neutron wavelength so that the scattered wave is spherical; and neglect of neutron magnetic scattering. Under these assumptions the ratio (2.1) can be computed (GRAY *et al.*, 2011; LOVESEY, 1984; SQUIRES, 1996) (via first-order perturbation theory in the first Born approximation in conjunction with linear superposition of scattered waves) for a system of many nuclei, say one mole, of a *simple* molecular fluid with N atoms (polyatomic system), volume V, at statistical temperature T as

$$\frac{d\sigma}{d\Omega}(\boldsymbol{q}) = \sum_{i=1}^{N}\sum_{j=1}^{N} \overline{b_i\, b_j} \left\langle e^{\imath\, \boldsymbol{q}\cdot\boldsymbol{x}_{\overrightarrow{ij}}} \right\rangle_{\mathrm{NVT}} , \tag{2.3}$$

where $\overline{b_i\, b_j}$ is the spin-isotopic average of the product of the bound scattering lengths (here assumed purely real) of nuclei i and j, respectively, and the structure term $\big\langle(\cdot)\big\rangle_{\mathrm{NVT}}$ is the classical statistical mechanics Gibbs' canonical ensemble average. In this result, the scattering vector $\boldsymbol{q} := \boldsymbol{k}_{\mathrm{S}} - \boldsymbol{k}_0$ is used instead of the direction $\hat{\boldsymbol{s}}$ as in (2.1); here $\boldsymbol{k}_{\mathrm{S}} = 2\pi\hat{\boldsymbol{s}}/\lambda$ is the scattered neutron wavevector with λ denoting the neutron wavelength (a constant in elastic scattering conditions), and $\boldsymbol{k}_0$ is the plane-wave incident wavevector. The vectors $\boldsymbol{x}_{\overrightarrow{ij}} := \boldsymbol{x}_j - \boldsymbol{x}_i$ point *from* atom i *to* atom j, for all pairs of atoms in the polyatomic ensemble; say i may represent an oxygen atom and j either another oxygen or a carbon atom, and so on. The left side of (2.3) is meant to be the real part of the right side.

The absolutely calibrated differential cross section (2.2) can be now approximated by its theoretical counterpart (2.1) as

$$\frac{d\Sigma}{d\Omega}(\boldsymbol{q}) \approx V^{-1}\frac{d\sigma}{d\Omega}(\boldsymbol{q}) \ . \tag{2.4}$$

Additional insight into the form of (2.3) can be obtained in two forms of representations used by different authors. The differences are not always transparent, thus here we analyze the differences to help organize calculations and obtain insight. The first representation is based on observing that terms in the sum with $i = j$ do not depend on $\boldsymbol{q}$. The sum of these isotropic terms contribute as a constant flat value to

the differential scattering cross section; this is known as the self part ($\boldsymbol{q}$-independent, isotropic) while the remaining part is called distinct (anisotropic), that is

$$\frac{d\Sigma}{d\Omega}(\boldsymbol{q}) \approx \overbrace{\frac{1}{V}\sum_{i=1}^{N}\sum_{\substack{j=1\\ j\neq i}}^{N} \overline{b}_i\,\overline{b}_j \left\langle e^{\imath\,\boldsymbol{q}\cdot\boldsymbol{x}_{ij}^{\rightarrow}}\right\rangle_{\mathrm{NVT}}}^{\text{distinct}} + \overbrace{\frac{1}{V}\sum_{i=1}^{N}\overline{b_i^2}}^{\text{self}}\,, \tag{2.5}$$

where it is assumed that the nuclei are uncorrelated, thus $\overline{b_i\,b_j} = \overline{b}_i\,\overline{b}_j\ \forall\ i \neq j$, and $\overline{b}_i$ is the average value of the scattering length of nucleus i, called the coherent scattering length of nucleus i. In this representation the terms that contribute to spatial interference of the scattered neutron waves are all collected in one place, namely, distinct. Again, the distinct part is a real number, hence only the real part of the ensemble average in (2.5) is retained.

The second form of representation is based on decomposing the average of the product of the spin-isotopic variation of the atomic scattering length as follows

$$\overline{b_i\,b_j} = \overline{b}_i\,\overline{b}_j + \delta_{ij}\big(\overline{b_j^2} - \overline{b}_j^2\big)\,, \tag{2.6}$$

where δ_{ij} is the Kronecker delta, and $\big(b_i^{\mathrm{inc}}\big)^2 := \overline{b_i^2} - \overline{b}_i^2 = \mathrm{var}\,(b_i)$ the square of the incoherent scattering length. This does not make b_i^{inc} the standard deviation of the scattering length of nucleus i because the incoherent scattering length can be a negative number. Equation (2.6) effectively decomposes the mean of a product into the sum of the product of the means and its variance. The decomposition (2.6) is trivial for $i = j$ but only holds true for $i \neq j$ when the values of b_i and b_j for any atom pair i, j are uncorrelated; this is the same assumption used in (2.5). Substituting (2.6) into (2.3) and using (2.4) one obtains

$$\frac{d\Sigma}{d\Omega}(\boldsymbol{q}) \approx \underbrace{\frac{1}{V}\sum_{i=1}^{N}\sum_{j=1}^{N} \overline{b}_i\,\overline{b}_j \left\langle e^{\imath\,\boldsymbol{q}\cdot\boldsymbol{x}_{ij}^{\rightarrow}}\right\rangle_{\mathrm{NVT}}}_{\text{coherent}} + \overbrace{\frac{1}{V}\sum_{i=1}^{N}\big(b_i^{\mathrm{inc}}\big)^2}^{\text{incoherent}}\,, \tag{2.7}$$

where the first term on the right side is the coherent part, and the second term is the incoherent (isotropic; $\boldsymbol{q}$-independent) part. In this representation, the coherent terms do not all contribute to spatial-dependent interference; that is, the factors with $i = j$ are isotropic.

The foregoing can be further reorganized using the total *neutron* static structure factor (including intra- and inter-molecular structure) defined as

$$S_{\mathrm{n}}(\boldsymbol{q}) := \frac{1}{\sum_{i=1}^{N}\overline{b}_i{}^2}\sum_{i=1}^{N}\sum_{j=1}^{N} \overline{b}_i\,\overline{b}_j \left\langle e^{\imath\,\boldsymbol{q}\cdot\boldsymbol{x}_{ij}^{\rightarrow}}\right\rangle_{\mathrm{NVT}}\,, \tag{2.8}$$

where the $\sum_{i=1}^{N} \overline{b}_i^2$ factor is preferred over other definitions found in the literature such as $\left(\sum_{i=1}^{N} \overline{b}_i\right)^2$ since $\sum_{i=1}^{N} \overline{b}_i$ may be very small for some samples. In fact, $N^{-1} \sum_{i=1}^{N} \overline{b}_i^2 = (4\pi)^{-1} \sum_{\alpha=1}^{M} w_\alpha \sigma_\alpha^{\mathrm{coh}}$, which is a more natural atom-fraction-weighted form as it is based on the α-nucleus total neutron scattering cross section, σ_α. Using the incoherent nucleus cross section definition $\sigma_i^{\mathrm{inc}} := 4\pi \left(b_i^{\mathrm{inc}}\right)^2 = 4\pi \ \mathrm{var}(b_i)$, and its arithmetic mean over all nuclei $\overline{\sigma}^{\mathrm{inc}} := N^{-1} \sum_{i=1}^{N} \sigma_i^{\mathrm{inc}} = \sum_{\alpha=1}^{M} w_\alpha \sigma_\alpha^{\mathrm{inc}}$; likewise for the coherent cross section $\sigma_i^{\mathrm{coh}} := 4\pi \left(\overline{b}_i\right)^2$ and $\overline{\sigma}^{\mathrm{coh}} := N^{-1} \sum_{i=1}^{N} \sigma_i^{\mathrm{coh}} = \sum_{\alpha=1}^{M} w_\alpha \sigma_\alpha^{\mathrm{coh}}$, then (2.5) becomes

$$\boxed{\frac{d\Sigma}{d\Omega}(\boldsymbol{q}) \approx \left(\frac{d\Sigma}{d\Omega}(\boldsymbol{q})\right)_{\mathrm{dist}} + \left(\frac{d\Sigma}{d\Omega}\right)_{\mathrm{self}}}, \text{with} \tag{2.9a}$$

$$\left(\frac{d\Sigma}{d\Omega}(\boldsymbol{q})\right)_{\mathrm{dist}} := \frac{n}{4\pi} \overline{\sigma}^{\mathrm{coh}} \left(S_{\mathrm{n}}(\boldsymbol{q}) - 1\right) , \text{and} \tag{2.9b}$$

$$\left(\frac{d\Sigma}{d\Omega}\right)_{\mathrm{self}} := \frac{n}{4\pi} \overline{\sigma} , \tag{2.9c}$$

where $n := N/V$ is the atom number density, $\overline{\sigma}^{\mathrm{coh}}$ is average coherent cross section of the sample, and $\overline{\sigma} = \overline{\sigma}^{\mathrm{coh}} + \overline{\sigma}^{\mathrm{inc}}$ the total average cross section of the sample. Relation (2.9a) reflects the comparison of the experimental value on the left, measured in absolute units, to the theoretical approximation on the right. Also, it explicitly shows that the differential scattering cross section is directly proportional to the number density of atoms, and it is the sum of a distinct anisotropic part, (2.9b), and a constant isotropic part, (2.9c); more on this topic later.

Likewise, using (2.8), (2.7) becomes

$$\boxed{\frac{d\Sigma}{d\Omega}(\boldsymbol{q}) \approx \left(\frac{d\Sigma}{d\Omega}(\boldsymbol{q})\right)_{\mathrm{coh}} + \left(\frac{d\Sigma}{d\Omega}\right)_{\mathrm{inc}}}, \text{with} \tag{2.10a}$$

$$\left(\frac{d\Sigma}{d\Omega}(\boldsymbol{q})\right)_{\mathrm{coh}} := \frac{n}{4\pi} \overline{\sigma}^{\mathrm{coh}} S_{\mathrm{n}}(\boldsymbol{q}) , \text{and} \tag{2.10b}$$

$$\left(\frac{d\Sigma}{d\Omega}\right)_{\mathrm{inc}} := \frac{n}{4\pi} \overline{\sigma}^{\mathrm{inc}} , \tag{2.10c}$$

where $\overline{\sigma}^{\mathrm{inc}}$ is the incoherent average cross section of the sample. Therefore (2.9) and (2.10) are slightly different ways of decomposing (2.3) where

$$\boxed{\left(\frac{d\Sigma}{d\Omega}(\boldsymbol{q})\right)_{\mathrm{coh}} = \left(\frac{d\Sigma}{d\Omega}(\boldsymbol{q})\right)_{\mathrm{dist}} + \frac{n}{4\pi} \overline{\sigma}^{\mathrm{coh}}} , \tag{2.11a}$$

and

$$\boxed{\left(\frac{d\Sigma}{d\Omega}\right)_{\text{inc}} = \left(\frac{d\Sigma}{d\Omega}\right)_{\text{self}} - \frac{n}{4\pi}\overline{\sigma}^{\text{coh}}}\,, \tag{2.11b}$$

demonstrating that distinct and self parts of (2.3) differ from the coherent and incoherent parts by a constant factor $\frac{n}{4\pi}\overline{\sigma}^{\text{coh}}$ proportional to the average atomic coherent scattering cross section of the sample material. Therefore per (2.11a) the measured scattering interference (coherent part) has two components, namely, distinct (anisotropic) and a self-interference (*i.e.* isotropic self-coherence).

The significance of (2.9) or (2.10) is to motivate the interpretation of a directly measured experimental macroscopic differential scattering cross section in terms of a neutron static structure factor by rearranging as

$$S_{\text{n}}(\boldsymbol{q}) \approx \frac{1}{\overline{\sigma}^{\text{coh}}}\left(\frac{4\pi}{n}\,\frac{d\Sigma}{d\Omega}(\boldsymbol{q}) - \overline{\sigma}^{\text{inc}}\right)\,. \tag{2.12}$$

The left side of the approximation is taken as the definition of a experimentally measured quantity and it is therefore considered as *directly* measured. This quantity is not a true structure factor because it contains neutron-nuclei interactions; the only exception when S_{n} reduces to a true structure factor is noted later for monoatomic systems.

2.1 Polyatomic structure factor

It is instructive to separate the contributions of the neutron-nuclei interaction from the atom-atom (structure) interaction in (2.9) and (2.10); note that all these interactions are mixed into the $\boldsymbol{q}$-dependent term on the right side. To obtain this separation, it is sufficient to perform the double sum in (2.8) over pairs of atoms of distinct type so that the $\overline{b}_i$'s and $\overline{b}_j$'s factor out of the sum effectively separating the atom-atom interaction term from the neutron-nuclei interaction coefficients, *i.e.* the $\overline{b}_i$'s. After that, all we have to do is to sum over all pairs of atom types. To this end we arrange the atoms by their types and denote them as $\alpha, \beta, \ldots$ such that the total number of atoms equals the sum of partial atom types, N_α, thus $N = \sum_{\alpha=1}^{M} N_\alpha$, with M denoting the number of nuclei types. Next we define the *neutron* partial static structure factors (not a true structure factor)

$$S^{\text{n}}_{\alpha\beta}(\boldsymbol{q}) := 4\pi\,\sqrt{w_\alpha\, w_\beta}\;\frac{\overline{b}_\alpha \overline{b}_\beta}{\overline{\sigma}^{\text{coh}}}\;S_{\alpha\beta}(\boldsymbol{q}), \tag{2.13}$$

where the α-nuclei atomic fraction is denoted $w_\alpha := N_\alpha/N$, and $S_{\alpha\beta}(\boldsymbol{q})$ is the true partial static structure factor

$$\boxed{S_{\alpha\beta}(\boldsymbol{q}) := \frac{1}{\sqrt{N_\alpha N_\beta}} \sum_{i=1}^{N_\alpha} \sum_{j=1}^{N_\beta} \left\langle e^{\imath\, \boldsymbol{q}\cdot\boldsymbol{x}_{\overrightarrow{\alpha_i\beta_j}}} \right\rangle_{\mathrm{NVT}}} \,, \tag{2.14}$$

which depends only on the distribution of the α atoms around the β atoms and vice-versa; this contains only genuine structural information including the dominant intra-molecular structure at short wavelengths. Here the vector pointing *from* the ith α atom *to* the jth β atom is denoted as $\boldsymbol{x}_{\overrightarrow{\alpha_i\beta_j}}$ as the atom pair separation vector. Note that both the true and neutron partial static structure factors are symmetric, *i.e.* $S_{\alpha\beta} = S_{\beta\alpha}$ (and $S^{\mathrm{n}}_{\alpha\beta} = S^{\mathrm{n}}_{\beta\alpha}$) hence only $M(M+1)/2$ distinct factors exist. Using (2.13) and (2.14) the *neutron* static structure factor (2.8) can be rewritten as a weighted sum of partial static structure factors

$$S_{\mathrm{n}}(\boldsymbol{q}) = \sum_{\alpha=1}^{M} \sum_{\beta=1}^{M} S^{\mathrm{n}}_{\alpha\beta}(\boldsymbol{q}), \text{ or} \tag{2.15a}$$

$$S_{\mathrm{n}}(\boldsymbol{q}) = \frac{4\pi}{\overline{\sigma}^{\mathrm{coh}}} \sum_{\alpha=1}^{M} \sum_{\beta=1}^{M} \sqrt{w_\alpha\, w_\beta}\; \overline{b}_\alpha \overline{b}_\beta\, S_{\alpha\beta}(\boldsymbol{q}) \;. \tag{2.15b}$$

Note that the sum of cross terms in (2.15a) and (2.15b), $S^{\mathrm{n}}_{\alpha\beta} + S^{\mathrm{n}}_{\beta\alpha}$, $\beta \neq \alpha$, will equal $2\, S^{\mathrm{n}}_{\alpha\beta}$ in view of symmetry.

The partial contribution of the structure of any pair of atoms to the total structure of the fluid $S_{\mathrm{n}}(\boldsymbol{q})$ can be readily evaluated from (2.15b). The ability to computationally evaluate (2.15b) provides additional insight into experiments when limited to the collection of the total neutron structure factor (2.12) of the fluid.

Substituting (2.15b) into (2.10b) one obtains a very insightful approximation of the coherent part of the experimental macroscopic differential scattering cross section

$$\left(\frac{d\Sigma}{d\Omega}(\boldsymbol{q})\right)_{\mathrm{coh}} = n \sum_{\alpha=1}^{M} \sum_{\beta=1}^{M} \sqrt{w_\alpha\, w_\beta}\; \overline{b}_\alpha \overline{b}_\beta\, S_{\alpha\beta}(\boldsymbol{q}) \;. \tag{2.16a}$$

That is, the coherent part (anisotropic) is the linear combination of true partial static structural factors, wherein the coefficients contain all the information of the interaction between neutrons and nuclei. The partial structure factors only contain information of the structure of the fluid, that is, the relative position of atoms, their motion, the force between atoms and the temperature. The partial structure factors are independent of how neutrons interact with nuclei and also independent of any intrinsic property of the neutron (mass, energy, spin, *etc.*). The form (2.16a) effectively unravels the property of the polyatomic sample from the neutron-nuclei interactions into a sum of factorization terms. Its corresponding incoherent part (2.10c) is

$$\left(\frac{d\Sigma}{d\Omega}\right)_{\text{inc}} = \frac{n}{4\pi}\overline{\sigma}^{\text{inc}} = \frac{n}{4\pi}\sum_{\alpha=1}^{M} w_\alpha \sigma_\alpha^{\text{inc}}. \tag{2.16b}$$

When the scattering sample is an isotropic fluid, a well known simplification in scattering theory can be applied. Let the incident neutron wavevector $\boldsymbol{k}_0$ point in the direction of the polar axis of a spherical coordinate system centered at the sample barycenter. Then write the plane wave factor in spherical harmonics (Gray and Gubbins, 1984, Rayleigh expansion)

$$e^{\imath \boldsymbol{q}\cdot\boldsymbol{x}_{\overrightarrow{ij}}} = 4\pi \sum_{l=0}^{\infty}\sum_{m=-l}^{m=l} \imath^l \, j_l(q\, x_{\overrightarrow{\alpha_i\beta_j}})\, Y_{lm}^*(\theta_q,\phi_q)\, Y_{lm}(\theta_x,\phi_x)\,, \tag{2.17}$$

where $q := \left\|\boldsymbol{q}\right\|$, $x_{\overrightarrow{\alpha_i\beta_j}} := \left\|\boldsymbol{x}_{\overrightarrow{\alpha_i\beta_j}}\right\|$, and the pairs (θ_q,ϕ_q) and (θ_x,ϕ_x) are the polar and azimuthal angles of the vectors $\boldsymbol{q}$ and $\boldsymbol{x}_{\overrightarrow{ij}}$, respectively. Isotropy of the sample means that the partial structure factors (2.14) are independent of the azimuthal angles ϕ_q and ϕ_x in the fluid. For this to happen in (2.17) the spherical harmonics $Y_{lm}(\cdot)$ need to be independent of the azimuthal angles and this prompts $m = 0$ which makes $l = 0$ and the only surviving term is the zeroth order Bessel function times the zeroth order spherical harmonics $Y_{00} = 1/\sqrt{4\pi}$, giving

$$e^{\imath \boldsymbol{q}\cdot\boldsymbol{x}_{\overrightarrow{ij}}} = 4\pi\, j_0(q\, x_{\overrightarrow{\alpha_i\beta_j}})\, Y_{00}^2 = \frac{\sin\left(q\, x_{\overrightarrow{\alpha_i\beta_j}}\right)}{q\, x_{\overrightarrow{\alpha_i\beta_j}}}\ . \tag{2.18}$$

Substitution of (2.18) into (2.14) gives

$$S_{\alpha\beta}(q) = \frac{1}{\sqrt{N_\alpha N_\beta}}\sum_{i=1}^{N_\alpha}\sum_{j=1}^{N_\beta}\left\langle \frac{\sin\left(q\, x_{\overrightarrow{\alpha_i\beta_j}}\right)}{q\, x_{\overrightarrow{\alpha_i\beta_j}}}\right\rangle_{\text{NVT}}\ , \tag{2.19}$$

which is now a function of $q = \frac{4\pi}{\lambda}\sin\theta$ where θ is the half angle between $\boldsymbol{k}_S$ and $\boldsymbol{k}_0$. Note the limit: $\lim_{q\to\infty} S_{\alpha\beta}(q) = \delta_{\alpha\beta}$.

2.2 Monoatomic fluid

For monoatomic systems, (2.16) reduces to

$$\left(\frac{d\Sigma}{d\Omega}(\boldsymbol{q})\right)_{\text{coh}} = \frac{n}{4\pi}\sigma^{\text{coh}}\, S(\boldsymbol{q}) \;, \tag{2.20a}$$

$$S(\boldsymbol{q}) := \frac{1}{N}\sum_{i=1}^{N}\sum_{j=1}^{N}\left\langle e^{\imath\,\boldsymbol{q}\cdot\boldsymbol{x}_{\overrightarrow{ij}}}\right\rangle_{\text{NVT}} \;, \tag{2.20b}$$

and

$$\left(\frac{d\Sigma}{d\Omega}\right)_{\text{inc}} = \frac{n}{4\pi}\sigma^{\text{inc}} \;. \tag{2.20c}$$

Here, (2.20b) is the true structure factor of the monoatomic fluid which accounts for all nucleus-nucleus interactions without any consideration of neutron-nuclei counterpart which is separately included in the prefactor σ^{coh} of (2.20a). Note that (2.10b) has the same form of (2.20a) but the *neutron* structure factor S_{n}, (2.8), has both nucleus-nucleus and neutron-nuclei interactions included and it is not a genuine structure factor as S in (2.20b) is. The proper extension of (2.20) to polyatomic systems is (2.16) which requires the use of partial structure factors to accomplish the separation of atom-atom interactions from probe-atom interactions as is typically done for monoatomic system.

The structure factor is related to the pair correlation function of a monoatomic fluid as follows. Consider the monoatomic fluid case (2.20b) then

$$\begin{aligned} S(\boldsymbol{q}) &= 1 + \frac{1}{N}\sum_{i=1}^{N}\sum_{j\neq i}^{N}\left\langle e^{\imath\,\boldsymbol{q}\cdot\boldsymbol{x}_{\overrightarrow{ij}}}\right\rangle_{\text{NVT}} \\ &= 1 + \frac{1}{N}\sum_{i=1}^{N}\sum_{j\neq i}^{N}\int_{\mathbb{R}^3} e^{\imath\,\boldsymbol{q}\cdot\boldsymbol{x}}\left\langle\delta\big(\boldsymbol{x}-\boldsymbol{x}_{\overrightarrow{ij}}\big)\right\rangle_{\text{NVT}} d\boldsymbol{x} \;, \end{aligned} \tag{2.21}$$

where $\boldsymbol{x}$ is an arbitrary pair separation vector. For a homogeneous fluid, the ensemble average on the last line does not depend where the particular pair separation vector, $\boldsymbol{x}_{\overrightarrow{ij}}$, is in space, therefore it can be computed as

$$\boxed{\left\langle\delta\big(\boldsymbol{x}-\boldsymbol{x}_{\overrightarrow{ij}}\big)\right\rangle_{\text{NVT}} = \frac{n}{N-1}\, g^{(2)}\big(\boldsymbol{x},\overline{\boldsymbol{r}}_{ij}\big)} \;, \tag{2.22}$$

where $\overline{\boldsymbol{r}}_{ij} := (\boldsymbol{x}_j+\boldsymbol{x}_i)/2$ is the centroid position of the i–j atom pair, and $g^{(2)}(\boldsymbol{x},\overline{\boldsymbol{r}}_{ij})$ is the pair correlation function of two atoms separated by $\boldsymbol{x}$ with centroid at $\overline{\boldsymbol{r}}_{ij}$. The

double sum in (2.21) can be computed using (2.22), thus

$$\frac{1}{N}\sum_{i=1}^{N}\sum_{j\neq i}^{N}\Big\langle\delta\big(\boldsymbol{x}-\boldsymbol{x}_{\overrightarrow{ij}}\big)\Big\rangle_{\mathrm{NVT}} = \frac{n}{N(N-1)}\sum_{i=1}^{N}\sum_{j\neq i}^{N} g^{(2)}\big(\boldsymbol{x},\overline{\boldsymbol{r}}_{ij}\big) = \frac{n}{V}\int_{\mathbb{R}^3} g^{(2)}\big(\boldsymbol{x},\boldsymbol{r}\big)\,d\boldsymbol{r} = n\,g(\boldsymbol{x})\ , \quad (2.23)$$

with $g(\boldsymbol{x})$ denoting the pair correlation function for atoms separated by $\boldsymbol{x}$. In the limit of large N, the double sum in (2.23) for $g^{(2)}(\cdot,\cdot)$, evaluated on all centroids $\overline{\boldsymbol{r}}_{ij}$, converges to the integral over the whole configurational space $\mathbb{R}^3$. This was used to arrive at the final result, in (2.23), involving the pair correlation function for a homogeneous fluid. Substituting (2.23) into (2.21) gives

$$S(\boldsymbol{q}) = 1 + n\int_{\mathbb{R}^3} e^{\imath\,\boldsymbol{q}\cdot\boldsymbol{x}}\,g(\boldsymbol{x})\,d\boldsymbol{x} = 1 + n\int_{\mathbb{R}^3} e^{\imath\,\boldsymbol{q}\cdot\boldsymbol{x}}\,\big(g(\boldsymbol{x})-1\big)\,d\boldsymbol{x} + (2\pi)^3\,n\,\delta(\boldsymbol{q})\ ,$$

which is typically redefined by ignoring the delta peak in the forward direction, thus

$$S(\boldsymbol{q}) = 1 + i(\boldsymbol{q})\ , \quad (2.24)$$

$$i(\boldsymbol{q}) := n\int_{\mathbb{R}^3} e^{\imath\,\boldsymbol{q}\cdot\boldsymbol{x}}\,\big(g(\boldsymbol{x})-1\big)\,d\boldsymbol{x}\ , \quad (2.25)$$

where the last line defines the interference function. For an isotropic fluid, the structure factor and pair correlation function are further simplified to depend on the magnitudes q and $r := \big\|\boldsymbol{x}\big\|$, and not on the directions of $\boldsymbol{q}$ and $\boldsymbol{x}$, respectively. Hence by virtue of (2.18)

$$i(q) = 4\pi\,n\int_0^\infty \frac{\sin qr}{qr}\,\big(g_{\mathrm{r}}(r)-1\big)\,r^2\,dr\ ,$$

here $g_r(\cdot)$ is the direction-independent pair correlation function known as radial distribution function obtained by integrating $g(\boldsymbol{x})$ in all directions, *i.e.*, using spherical coordinates

$$g_{\mathrm{r}}(r) := \frac{1}{4\pi}\int_0^{2\pi} d\phi\int_0^{\pi}\sin\theta\,g(\boldsymbol{x})\,d\theta\ . \quad (2.26)$$

The limits at low q and high q are significant; using $\lim_{q\to 0}\frac{\sin qr}{qr} = 1$, and $\lim_{q\to\infty}\frac{\sin qr}{qr} =$

0 gives

$$\lim_{q\to 0} i(q) = 4\pi\, n \int_0^\infty \big(g_{\rm r}(r) - 1\big)\, r^2\, dr \Rightarrow \tag{2.27}$$

$$\lim_{q\to 0} S(q) = n\, k_B T\, \kappa_T = -\frac{n\, k_{\rm B} T}{V} \frac{\partial V}{\partial p}\Big|_T \,, \tag{2.28}$$

$$\lim_{q\to\infty} i(q) = 0 \;\Rightarrow\; \lim_{q\to\infty} S(q) = 1 \,.$$

The forward scattering limit (2.28) arises from large scale (relative to the molecular scale) density thermal fluctuation which is a function of the thermodynamic isothermal compressibility of the homogeneous, isotropic fluid, κ_T ($k_{\rm B}$ is the Boltzmann constant), that is, if $\overline{\nu}$ is the average number of atoms or particles in a small volume (large compared with the molecular scale), then it is possible to demonstrate that the relative fluctuation, $\frac{\mathrm{var}(\nu)}{\overline{\nu}} = \frac{\overline{\nu^2} - \overline{\nu}^2}{\overline{\nu}}$, is equal to (2.28) or from (2.27), $\frac{\mathrm{var}(\nu)}{\overline{\nu}} = 1 + 4\pi\, n \int_0^\infty \big(g_{\rm r}(r) - 1\big)\, r^2\, dr$. Note that only in a monoatomic fluid (2.28) can be used directly to obtain the isothermal compressibility of the fluid using $\lim_{q\to 0} S(q)$ from measurements if $\sigma^{\rm coh}$, $\sigma^{\rm inc}$, and n are known in (2.20). In a polyatomic fluid, what is measured is $S_{\rm n}(\boldsymbol{q})$ which is "not" a structure factor quantity since it depends on neutron-nuclei interaction.

For future reference, the relative atom number fluctuation can also be expressed in terms of the volume fluctuation

$$\frac{1}{n}\, \frac{\mathrm{var}(\nu)}{\overline{\nu}} = \frac{\overline{V^2} - \overline{V}^2}{\overline{V}} = k_{\rm B} T\, \kappa_T, \tag{2.29}$$

allowing for an expedient calculation of κ_T with MD simulations using an NPT ensemble.

2.3 Polyatomic fluid

For polyatomic systems similar extensions of (2.24) and (2.25) follows for the true partial structural factors:

$$\boxed{S_{\alpha\beta}(\boldsymbol{q}) = \delta_{\alpha\beta} + \sqrt{w_\alpha w_\beta}\; i_{\alpha\beta}(\boldsymbol{q}) \,,} \tag{2.30}$$

$$\boxed{i_{\alpha\beta}(\boldsymbol{q}) := n \int_{\mathbb{R}^3} e^{\imath\, \boldsymbol{q}\cdot\boldsymbol{x}} \big(g_{\alpha\beta}(\boldsymbol{x}) - 1\big)\, d\boldsymbol{x} \,,} \tag{2.31}$$

and

$$i_{\alpha\beta}(q) = 4\pi\, n \int_0^\infty \frac{\sin qr}{qr} \big(g_{{\rm r}\alpha\beta}(r) - 1\big)\, r^2\, dr \,,$$

where $g_{\mathrm{r}\alpha\beta}(\cdot)$ is the partial radial distribution function for an α-nucleus separated from a β-nucleus by a distance x, and $i_{\alpha\beta}(\cdot)$ the corresponding partial interference function (these are symmetric, $i_{\alpha\beta} = i_{\beta\alpha}$). Note the limits:

$$\lim_{q\to 0} i_{\alpha\beta}(q) = 4\pi\, n \int_0^\infty \big(g_{\mathrm{r}\alpha\beta}(r) - 1\big)\, r^2\, dr \ , \tag{2.32}$$

$$\lim_{q\to\infty} i_{\alpha\beta}(q) = 0 \ \Rightarrow \lim_{q\to\infty} S_{\alpha\beta}(q) = \delta_{\alpha\beta} \ . \tag{2.33}$$

In a polyatomic fluid, κ_T cannot be obtained from an experimental measurement of $S_{\mathrm{n}}(\boldsymbol{q})$ as explained earlier. However for a homogeneous, isotropic, fluid consisting of small, rigid molecules the center of mass structure factor, $S_{\mathrm{cm}}(\boldsymbol{q})$, can be computed in a similar way as in (2.20b) when using the separation of the center of mass of the molecules, $\boldsymbol{x}_{\overrightarrow{IJ}}$, in place of $\boldsymbol{x}_{\overrightarrow{ij}}$ and summing the plane wave factors over N_m molecules

$$S_{\mathrm{cm}}(\boldsymbol{q}) := \frac{1}{N_m} \sum_{I=1}^{N_m} \sum_{J=1}^{N_m} \Big\langle e^{\imath\, \boldsymbol{q}\cdot\boldsymbol{x}_{\overrightarrow{IJ}}} \Big\rangle_{\mathrm{NVT}},$$

this way, it can be shown that $\lim_{q\to 0} S_{\mathrm{cm}}(q) = m\, k_{\mathrm{B}} T\, \kappa_T$, where $m := N_m/V$ is the molecule number density. Since the center of mass is an arbitrary point within the molecule domain, any atom within the molecule can be chosen as a reference site, therefore any combination of atoms belonging to different molecules produces the inter-molecular structure factor

$$S^{\mathrm{inter}}_{\alpha\beta}(\boldsymbol{q}) := \frac{1}{N_m} \sum_{I=1}^{N_m} \sum_{J=1}^{N_m} \Big\langle e^{\imath\, \boldsymbol{q}\cdot\boldsymbol{x}_{\overrightarrow{\alpha_I\beta_J}}} \Big\rangle_{\mathrm{NVT}} \ , \tag{2.34}$$

which will deliver the same result in the forward scattering limit (only in this limit and not other values of q): $\lim_{q\to 0} S^{\mathrm{inter}}_{\alpha\beta}(q) = \lim_{q\to 0} S_{\mathrm{cm}}(q) = m\, k_{\mathrm{B}} T\, \kappa_T$ for any inter-molecular $\alpha\beta$ combination.

It is instructive to demonstrate how an experiment campaign can be designed to measure the partial structure factors of 1,4-dioxane using the isotopic substitution method. Combining (2.30) and (2.16), the differential scattering cross section (2.10) can be expressed as

$$\frac{d\Sigma}{d\Omega}(\boldsymbol{q}) \approx n \sum_{\alpha=1}^{M} \sum_{\beta=1}^{M} w_\alpha w_\beta\ \overline{b}_\alpha \overline{b}_\beta\ i_{\alpha\beta}(\boldsymbol{q}) \ + \ \frac{n}{4\pi}\overline{\sigma} \ , \tag{2.35}$$

which demonstrates that no single measurement of $\frac{d\Sigma}{d\Omega}$ will allow for the calculation of the partial pair correlation functions and their Fourier transforms, namely, the partial

structure factors. A method for enabling such a measurement uses k values of the normalized interference function defined as

$$\widehat{i}(\boldsymbol{q}) := \frac{\frac{d\Sigma}{d\Omega}(\boldsymbol{q}) - \frac{n}{4\pi}\overline{\sigma}}{\frac{n}{4\pi}\overline{\sigma}^{\mathrm{coh}}} \tag{2.36}$$

which leads to, using (2.35), the following linear system of equations for the unknown partial interference functions

$$\boxed{\sum_{\alpha=1}^{M}\left(c_\alpha^{(k)}\right)^2\, i_{\alpha\alpha}(\boldsymbol{q}) + 2\sum_{\alpha=1}^{M}\sum_{\beta>\alpha}^{M} c_\alpha^{(k)} c_\beta^{(k)}\, i_{\alpha\beta}(\boldsymbol{q}) = \widehat{i}_k(\boldsymbol{q}) \qquad k = 1,\ldots,M(M+1)/2\ ,} \tag{2.37}$$

with coefficients

$$c_\alpha^{(k)} := \sqrt{4\pi}\frac{w_\alpha^{(k)}\overline{b}_\alpha^{(k)}}{\sqrt{\overline{\sigma}^{\mathrm{coh}(k)}}}\ ,\ \alpha = 1,\ldots,M.$$

Therefore by making $M(M+1)/2$ measurements for $\widehat{i}_k(\boldsymbol{q})$ with different atomic fractions, $w_\alpha^{(k)}$, obtained by mixing different amounts of $C_4H_8O_2$ and $C_4D_8O_2$, the linear system of equations can be solved for all partial interference functions $i_{\alpha\beta}(\boldsymbol{q})$ (M $\alpha\alpha$ partials, and $M(M-1)/2$ cross $\alpha\beta$ partials) which can be Fourier transformed from (2.31) to give the partial pair correlation functions, or used directly in (2.30) to give the partial structure factors.

For a dioxane liquid, $M = 4$ (C,O,H,D), hence 10 measurements of $\widehat{i}_k(\boldsymbol{q})$ are necessary to determine the 10 partial structure factors. Therefore 10 sets of coefficients $c_\alpha^{(k)}$, $k = 1,\ldots,10$ would be needed with different mole fractions of deuterated and protiated dioxane. The particular choice of the fractions should be such that it renders the linear system (2.37) non-singular and well conditioned. This gives an idea of how complementary and helpful MD simulations can be. As we will see later, all partial structure factors can be computed with MD simulations and provide initial insight on the structure for the fluid prior to conduct an extensive experiment based on (2.37).

3 Methods

This work entailed experimental and computational components as described in the next two subsections. The experimental work focused on the small-q range, $5.35\times10^{-3}\,\text{Å}^{-1} \le q \le 1.51\,\text{Å}^{-1}$, and the computational work focused on the small-to-wide range, $6.0\times10^{-2}\,\text{Å}^{-1} \le q \le 10\,\text{Å}^{-1}$.

3.1 Small-angle neutron scattering

Deuterated 1,4-dioxane-d_8 (D, 99%) was purchased from Cambridge Isotope Laboratories Inc. USA, and Sigma-Aldrich USA, and loaded, as received, into quartz banjo cells with 20 mm in diameter and 1 mm-thickness. They were exposed to the neutron beam of the time-of-flight, extended-q, small-angle scattering diffractometer, EQ-SANS (beam line 6), at the Spallation Neutron Source (SNS) (Zhao, 2000, 2001). The sample to detector distance was 1.3 m, choppers operated at 30 Hz in frame-skipping mode (Zhao *et al.*, 2010). The bands of neutrons passed in each frame were 2 to 6.3 Å and 10.6 to 14.9 Å which covered the range $5.35 \times 10^{-3}\,\text{Å}^{-1} \leq q \leq 1.51\,\text{Å}^{-1}$. The neutron beam was 10 mm in diameter, and the SNS target station power during data collection was 939.5 MW (60 Hz). Data was acquired for 170 s for transmission and 3400 s for scattering at two temperatures, namely, 25 °C and 70 °C. Reduction and scaling of the data in absolute units was done according to instrument protocol (Do *et al.*, 2014; Zhao *et al.*, 2010). Additional measurements were made with: empty camera, empty quartz cell, and Porasil B standard for instrument corrections done by automated software including adjustments for sensitivity, flight-path correction, background, and absolute unit scaling. The differential scattering cross section $\frac{d\Sigma}{d\Omega}$ was then averaged in azimuthal angle and presented as a function of q.

3.2 Classical molecular dynamics simulation

The all-atom force field for 1,4-dioxane used in this work was advanced by Cinacchi *et al.* (see their supplementary information for parameters and description). The same force field was used for either a deuterated or protiated system and their mixtures. The molecular dynamics simulation code LAMMPS (Plimpton, 1995) implements the needed components of this force field and was employed in this work. A system consisting of 6400 dioxane molecules ($N = 89600$) was setup in a periodic simulation box with initial configuration obtained from the Packmol tool (Martínez *et al.*, 2009). Input data files were written for LAMMPS including scripts for carrying out a sequence of ensemble calculations to obtain equilibrium trajectories. The system was heated and equilibrated at 500 K with an NVT ensemble simulation for 1 ns, then let cool down with steps of intervening NVT simulations to reach the final temperatures needed. Finally an isothermal-isobaric (NPT) ensemble simulation was performed at 1 bar where mass density was computed (table 3.1) for different temperatures. A Nosé-Hoover thermostat and barostat (Plimpton, 1995) were used to control temperature and pressure, with a time constant of 0.1 and 1.0 ps, respectively. Canonical (NVT) ensemble simulations then followed using an initial configuration from the NPT simulation at equilibrium. This allows for consistent atomic trajectories of the NVT and NPT ensembles, enabling the verification of (2.28) using (2.29), which

Table 3.1: *Mass density ρ [g cm^{-3}] of dioxane $C_4H_8O_2$.*

T [K]	MD sim.	Exp't(CONTRERAS S, 2001)	Error [%]
298	1.01	1.028	−1.75
318	0.98	1.005*	−2.49
343	0.95	0.977*	−2.76

* Extrapolated.

requires an NPT ensemble, and (2.20b), which requires an NVT ensemble. A force potential cutoff of 12 Å was used for Lennard-Jones interactions with common tail corrections; Coulombic interactions were handled with the particle-particle particle-mesh method. The SHAKE (PLIMPTON, 1995) algorithm was used to constrain bond lengths in the dioxane molecules. At each statistical temperature (298.15 K, 318.15 K, and 343.15 K) at a constant pressure of 1 bar, the system was equilibrated for at least 1 ns (using a fixed time step of 1 fs), and atomic trajectories of at least an additional 5 ns elapsed time were used for analysis. We ensured that elapsed times were sufficient for the system to reach a diffusive regime at all temperatures, and verified that no correlated motion existed by computing the intermediate scattering function for various q values; the later decayed to zero in less than 1 ns.

The simulated thermal expansion $\alpha_p := -\frac{1}{\rho}\frac{\partial \rho}{\partial T}\big|_p$ was computed as $1.3 \times 10^{-3}\,\mathrm{K}^{-1}$ at 298K consistent with the experimental result $1.1 \times 10^{-3}\,\mathrm{K}^{-1}$(CONTRERAS S, 2001) (18.2 % error). The heat capacity $c_p := \frac{\partial \langle H \rangle}{\partial T}\big|_p$ could be computed from the slope of the NPT ensemble averaged enthalpy variation with temperature but such treatment leads to significant overestimate of c_p. We obtained $336.5\,\mathrm{J\,mol^{-1}\,K}$; much larger than the experimental value of $150.6\,\mathrm{J\,mol^{-1}\,K^{-1}}$(BROCOS *et al.*, 1999). The source of this error is the poor prediction of the molecular configuration enthalpy (*i.e.* molecular vibration) by typical MD force fields. Here the enthalpy is decomposed into the sum of an ideal component and a residual component (LIU AND MAGINN, 2011). The former is obtained either from experiments or *ab initio* simulations, and the latter is obtained in two ways. First, from classical NPT MD simulations via $c_p^{\mathrm{res}} := \frac{1}{k_B T^2}\big\{\langle U^{\mathrm{NB}}\hat{H}\rangle - \langle U^{\mathrm{NB}}\rangle\langle \hat{H}\rangle + p\big(\langle V\hat{H}\rangle - \langle V\rangle\langle\hat{H}\rangle\big)\big\} - R$, where U^{NB} is the intermolecular non-bonded potential energy, $\hat{H} = U + pV$ is the configuration enthalpy, and R the ideal gas constant. Second, from the slope of the residual enthalpy $H^{\mathrm{res}} = U^{\mathrm{NB}} + pV - Nk_BT$ as a function of temperature, $c_p^{\mathrm{res}} = \frac{\langle H^{\mathrm{res}}\rangle}{\partial T}\big|_p$. The two methods were pursued in this work, the first produced $c_p^{\mathrm{res}} = 68\,\mathrm{J\,mol^{-1}\,K^{-1}}$ and the second method, $c_p^{\mathrm{res}} = 72.6\,\mathrm{J\,mol^{-1}\,K^{-1}}$. When added to the ideal heat capacity(HARRISON AND SEATON, 1988), $c_p^{\mathrm{ideal}} = 94.1\,\mathrm{J\,mol^{-1}\,K^{-1}}$, the average simulated heat capacity

was $164.4\,\mathrm{J\,mol^{-1}\,K^{-1}}$ (9.16 % error).

We tested predictions of self diffusivity D by computing the mean square distance (MSD) of m molecules in conjunction with Einstein's relation $D := \frac{1}{6}\lim_{t\to\infty}\frac{d}{dt}\left\langle \sum_{i=1}^{m}\big(\boldsymbol{x}_i(t)-\boldsymbol{x}_i(0)\big)^2\right\rangle$ where $\boldsymbol{x}_i(t)-\boldsymbol{x}_i(0)$ is the displacement of the center of mass of the ith molecule at time t relative to its position at time $t=0$. The linear regime of variation of the MDS with time (*i.e.* diffusive regime) was computed for several temperatures and the constant slope D evaluated to give very good results as compared to experimental values (table 3.2). The activation energy of diffusion, E_D, obtained by fitting Arrhenius' formula, $D = D_0\, e^{-\frac{E_D}{RT}}$, to the simulation data (table 3.2), $13.3\,\mathrm{kJ\,mol^{-1}}$, is in excellent agreement with the experimental value $13.9\,\mathrm{kJ\,mol^{-1}}$ (−4.32 % error).

Table 3.2: *Self diffusivity D [$10^{-9}\,m^2\,s^{-1}$] of dioxane $C_4H_8O_2$.*

T [K]	MD sim.	Exp't(Holz *et al.*, 2000)	Error [%]
298	1.07	1.089	−1.74
318	1.56	1.561	−0.06
343	2.2	2.407*	−8.6

* Extrapolated.

The isothermal compressibility of dioxane can be computed by MD simulations in at least two ways, namely, either using a series of NPT simulations at different pressures to obtain $\kappa_T := -\frac{1}{V}\frac{\partial V}{\partial p}\big|_T$ by finite differences, or using (2.29) to compute $\kappa_T = \frac{\overline{V^2}-\overline{V}^2}{\overline{V}}\frac{1}{k_\mathrm{B}T}$ within a single NPT MD simulation. We employed the latter option and obtained good agreement with experimental data (table 3.3). More importantly,

Table 3.3: *Isothermal compressibility κ_T [GPa^{-1}] of dioxane $C_4H_8O_2$.*

T [K]	MD sim.	Exp't(Villares *et al.*, 2004)	Error [%]
298	0.732	0.759	−3.56
318	0.983	0.873*	−11.19
343	1.24	—	—

* Extrapolated.

we establish that the isothermal compressibility increases with increasing temperature, thus the structure factor of the fluid (2.28) will also do so at $q = 0$; more on this later.

For later comparison with the structure factor calculations we computed (HUMPHREY *et al.*, 1996) the inter-molecular radial distribution function $g_{\mathrm{COM}}(r)$ (2.26) for the dioxane molecular center of mass (COM), and several partial radial distribution functions $g_{\alpha\beta}$ (2.31) (fig. 3.1). Dioxane is a classical van der Waals liquid (inset of fig. 3.1) with an average coordination shell period of about 4.7 Å. The intra-molecular cor-

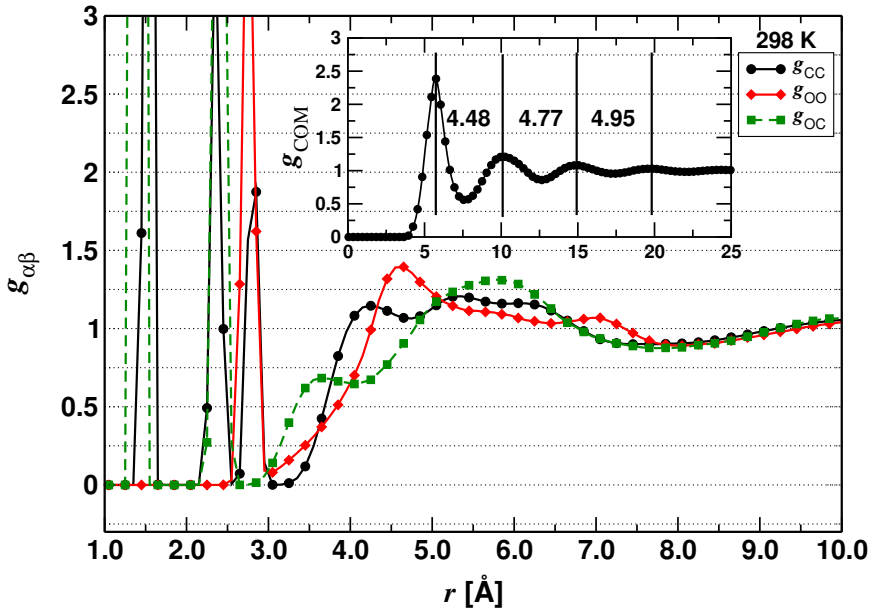

Fig. 3.1: *Computed (MD) radial distribution function of the molecular center of mass of 1,4-dioxane (inset), and several partial radial distribution functions including intra-molecular correlation peaks ($r < 3$ Å).*

relations of atom pairs generate salient peaks in $g_{\mathrm{COM}}(r)$ at $r < 3$ Å (fig. 3.1). The origin of three CC peaks, two OC peaks and one OO peak can be identified with the chair conformation of the 1,4-dioxane molecule. The dioxane molecule coordination number is defined as $\frac{N_m}{V}\int_0^{r_1} 4\pi r^2 g_{\mathrm{COM}}(r)\,dr$, where $r_1 = 7.6$ Å is the first minimum of $g_{\mathrm{COM}}(r)$. The calculated coordination is found to be 12.6 which indicates that about 12–13 molecules, in average, surround any given dioxane molecule.

A central calculation procedure in this work is the computation of the static partial structure factors (2.14), which can be more efficiently computed in the form

$$\begin{aligned} S_{\alpha\beta}(\boldsymbol{q}) &= \frac{\langle A_\alpha^* A_\beta\rangle}{\sqrt{N_\alpha N_\beta}}\ , \\ &= \frac{\delta_{\alpha\beta}\langle |A_\alpha|^2\rangle + (1-\delta_{\alpha\beta})\langle A_\alpha^* A_\beta\rangle}{\sqrt{N_\alpha N_\beta}}\ , \end{aligned} \tag{3.1}$$

where $A_\alpha := \sum_{i=1}^{N_\alpha} e^{\imath\, \boldsymbol{q}\cdot\boldsymbol{x}_{\alpha_i}}$, and the complex conjugate product notation, $A_\alpha^* A_\beta$, is meant to be its real part. The efficiency arises from using the product of two sums ($\mathcal{O}(N_\alpha + N_\beta)$ operations) instead of a double sum as in (2.14) ($\mathcal{O}(N_\alpha N_\beta)$ operations). Note that when $\alpha = \beta$, (3.1) is clearly a non-negative real number. In view of the periodic boundary conditions imposed in the simulation domain, the direct calculation of (3.1) can only be made at wave vectors multiple of $\frac{2\pi}{L}$ with L the length of the simulation cubic domain with volume V. Therefore $\boldsymbol{q} = \frac{2\pi}{L}(q_1, q_2, q_3),\ q_1, q_2, q_3 = 1, 2, \ldots N_q$ which sets a severe lower bound on q, that is, in our case $q_{\min} = \frac{2\pi}{97.54\,\text{Å}} = 0.064\,\text{Å}^{-1}$. The upper bound was chosen so to extend to $q_{\max} = 10\,\text{Å}^{-1}$ hence $N_q = 156$ where a total of $N_q^3 = 3\,796\,416$ scattering vectors, $\boldsymbol{q}$, are available; of those we used only $3N_q$ as $\frac{2\pi}{L}(i, 0, 0)$,$\frac{2\pi}{L}(0, i, 0)$, and $\frac{2\pi}{L}(0, 0, i)$, $i = 1, \ldots, N_q$.

Once partial structure factors are at hand, the corresponding differential scattering cross section can be computed through (2.9) or (2.10) using the total neutron static structure factor (2.15); values for needed atomic scattering lengths are readily available (table 3.4). We performed all calculations involving (3.1) with our own

Table 3.4: *Bound neutron scattering lengths for atoms in dioxane (NIST website* `www.nist.gov`*). The mole fraction of $C_4H_8O_2$ in $C_4D_8O_2$ is denoted x, hence a 99% deuterated sample has $x = 0.01$. The α-nuclei atomic fraction w_α assumes a dioxane molecule is either fully deuterated or fully protiated. Coherent and incoherent cross sections for deuterated dioxane $C_4D_8O_2$ and protiated $C_4H_8O_2$ are listed at the foot of the table.*

α-atom	w_α	$\overline{b}_\alpha$ [fm]	b_α^{inc} [fm]
O	1/7	5.803	0
C	2/7	6.6511	0
D	$\frac{4}{7}(1-x)$	6.671	4.04
H	$\frac{4}{7}x$	−3.7406	25.274
$\overline{\sigma}_{\text{d8}}^{\text{coh}} = 5.388\,\text{b}$		$\overline{\sigma}_{\text{d8}}^{\text{inc}} = 1.172\,\text{b}$	
$\overline{\sigma}_{\text{h8}}^{\text{coh}} = 3.198\,\text{b}$		$\overline{\sigma}_{\text{h8}}^{\text{inc}} = 45.869\,\text{b}$	

computer codes.

In order to test our scattering calculation approach we computed κ_T of dioxane, $C_4H_8O_2$, using (2.34) and its limit $\kappa_T = \frac{1}{m\, k_B T} \lim_{q\to 0} S_{\alpha\beta}^{\text{inter}}(q)$ for different temperatures and different atom pairs, namely OO, CC, OC. The results (table 3.5) only varied with temperature as expected, they were in very good agreement with experimental values and the results from direct molecular dynamics simulations (table 3.3). We expect the scattering-based results for κ_T to be improved with a greater sampling of the $\boldsymbol{q}$ space, and with an increase of the MD simulation box so $q_{\min}$ is further

reduced. As discussed earlier, this is a very expensive computational exercise. For instance, to access a mere $q_{\min} = 0.01\,\text{Å}^{-1}$, the MD box length would increase by a factor of 6.4 leading to a simulation with over 23 million atoms.

Table 3.5: *Isothermal compressibility κ_T [GPa^{-1}] of dioxane $C_4H_8O_2$ calculated via neutron scattering on MD trajectories.*

T [K]	$\frac{1}{m\,k_B T}\lim_{q\to 0} S^{\text{inter}}_{\text{OO}}(q)$	Error [%]*
298	0.67	−8.47
318	0.888	−9.66
343	1.3	4.84

* Relative to direct MD results (table 3.3).

4 Results and discussion

Liquid 1,4-dioxane is a low intensity scatterer as indicated by the magnitude of $\frac{d\Sigma}{d\Omega}$ (fig. 4.1). Static differential scattering cross sections were obtained (fig 4.1) in the extended q range for two temperatures, namely, 298.15 K and 343.15 K in the SANS-q range for the two samples purchased from different vendors. The large-q range data at 298.15 K with WANS was reproduced from BAKO *et al.* The variability of results with vendor sample is indicated in the graph of $\frac{d\Sigma}{d\Omega}$ in the small-q range.

For comparison, our fully deuterated MD simulation curve of $\frac{d\Sigma}{d\Omega}$ computed from (2.10), (2.15a) and (3.1) (see sec. 3.2) is superimposed on the experimental data (fig. 4.1) demonstrating excellent agreement with both the SANS and WANS data near the first structural peak. The peak is located at $q_1 = 1.37\,\text{Å}^{-1}$ which corresponds to a separation distance of $d = \frac{2\pi}{q_1} = 4.6\,\text{Å}$. This value is in close agreement with the average coordination shell period of 4.7 Å (fig. 3.1). The primary peak width of $\frac{d\Sigma}{d\Omega}$ is measured as $0.36\,\text{Å}^{-1}$ (fig. 4.1), that is, the full width at the half peak maximum indicates what the correlation length of the system should be, thus $\frac{2\pi}{0.36\,\text{Å}^{-1}} = 17.5\,\text{Å}$ which agrees with the point where the oscillations of the COM radial distribution function begin to die off (fig. 3.1). Hence, here too great agreement between MD simulations and measured neutron scattering is obtained.

The encouraging aforementioned results are moderated by striking discrepancies between measurements and simulations. First, there is the departure of the SANS data from the WANS data on the left side ($q \approx 1\,\text{Å}^{-1}$) of the first structural peak followed by a convex upturn in the $0.6\,\text{Å}^{-1} \le q \le 1\,\text{Å}^{-1}$ range with an inflection to a concave smaller-q range ($q \le 0.6\,\text{Å}^{-1}$). Note that in spite of the reduced accuracy

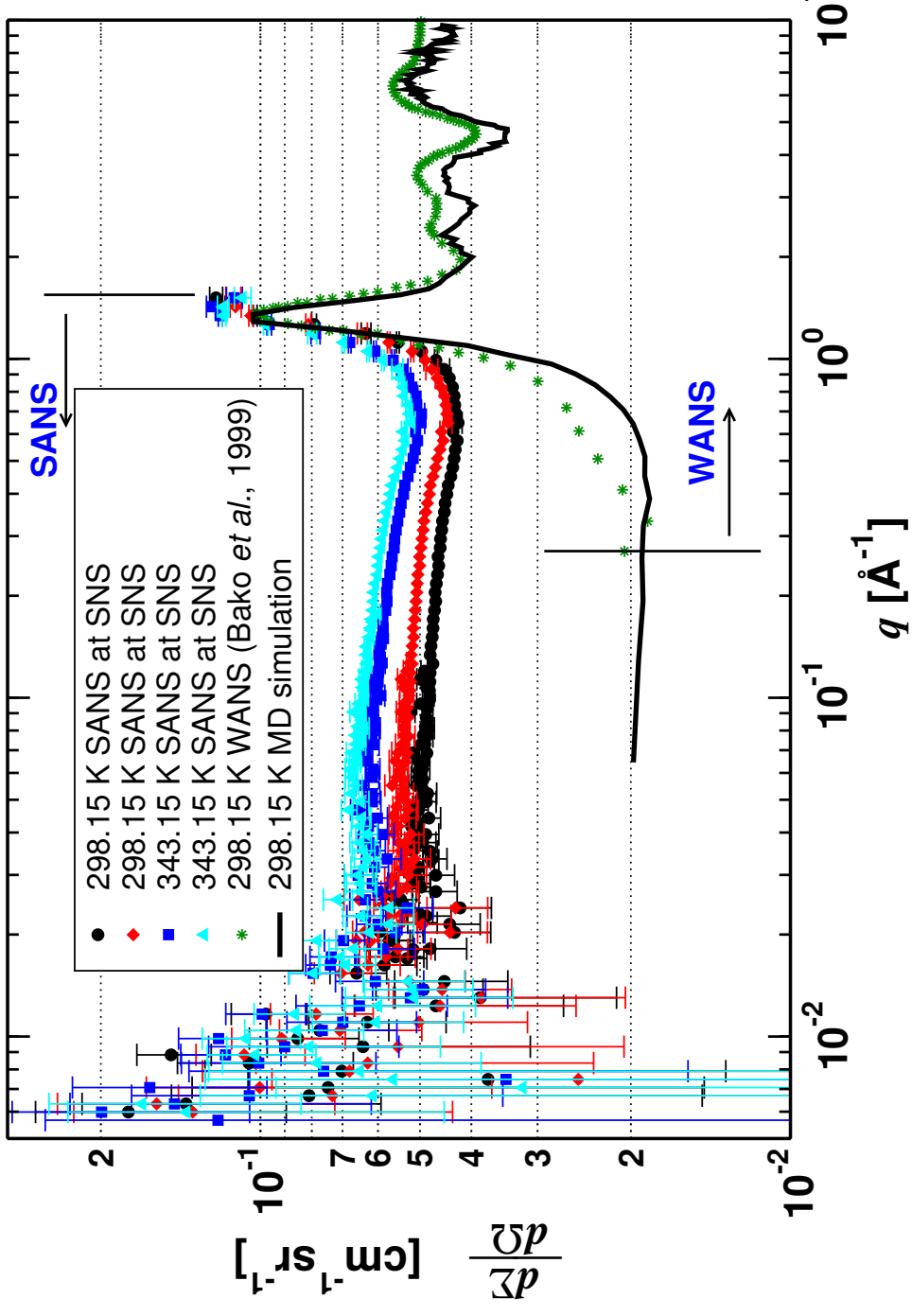

Fig. 4.1: *Differential scattering cross section for 1,4-dioxane in absolute units. The disagreement between experimental data and MD simulation is explained in the text as a result of protiated dioxane impurity or other hydrogen contamination (figs. 4.2 and 4.15).*

of the WANS data in the small-q region, there is good agreement with the MD simulation results on the left side of the peak and the peak's position. A concave trend in the small-q range is also observed in the MD simulation results but with a glaring vertical shift. In addition, the peak's height and position of the SANS data are not in agreement with the WANS data because $q > 1\,\text{Å}^{-1}$ is at the limits of the instrument range and difficult to properly normalize. That is to say, the WANS data should be more reliable than the SANS data. A second observation is that on the large-q range, to the right of the first structural peak, the simulation results also seem shifted downward but much less than the shift observed in the small-q range.

We investigated these issues by performing MD simulations of systems with increased content of protiated dioxane to elucidate the non-uniform shifting of the scattering intensity with respect to the simulation results (fig. 4.2). Here a dioxane

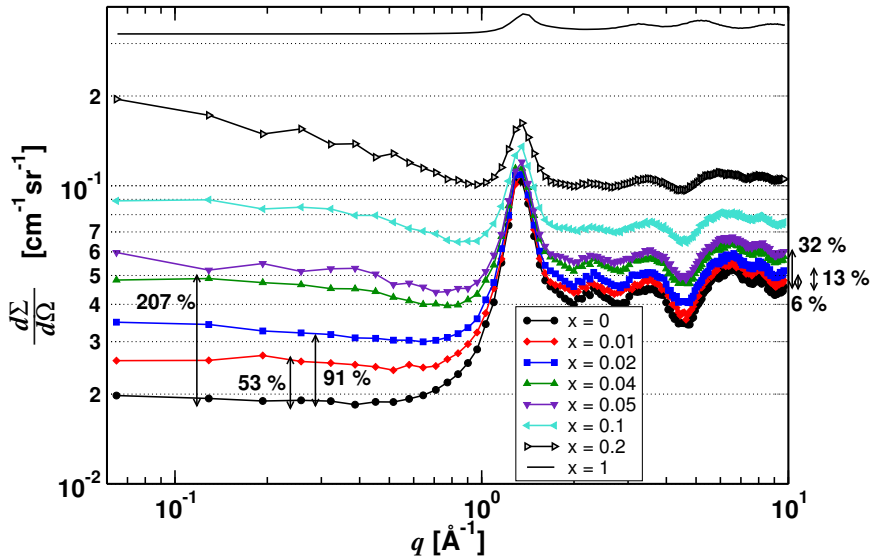

Fig. 4.2: *MD simulation results with increased molar fraction of protiated dioxane at 298 K. Note that the upward shift of curves is not just a vertical translation at small-q; this indicates that coherent effects are present.*

molecule is simulated either fully deuterated or fully protiated. The simulations were carried out with the same force field parameters for all levels of deuteration, therefore it is the interaction of neutrons and atoms, via the atomic scattering length, and molar fractions, and selected partial structure factors (shown later) that affect the resulting scattering.

By virtue of (2.10) and (2.16), the differential scattering cross section is

$$\boxed{\frac{d\Sigma}{d\Omega}(\boldsymbol{q}) \approx n \sum_{\alpha=1}^{M} \sum_{\beta=1}^{M} \sqrt{w_\alpha\, w_\beta}\; \bar{b}_\alpha \bar{b}_\beta\, S_{\alpha\beta}(\boldsymbol{q}) + \frac{n}{4\pi} \overline{\sigma}^{\mathrm{inc}},} \tag{4.1}$$

where the results obtained (fig. 4.2) demonstrate that the incoherence background dominates the variation of $\frac{d\Sigma}{d\Omega}$ in the large-q range for all molar fractions of protiated dioxane. That is, increasing levels of protiated dioxane lead to a uniform vertical shift of $\frac{d\Sigma}{d\Omega}$ in the large-q range. Here the incoherent background for a fully deuterated system is $\frac{n}{4\pi}\overline{\sigma}^{\mathrm{inc}}_{\mathrm{d8}} = 9 \times 10^{-3}\,\mathrm{cm}^{-1}\,\mathrm{sr}^{-1}$, and $\frac{n}{4\pi}\overline{\sigma}^{\mathrm{inc}}_{\mathrm{h8}} = 0.352\,\mathrm{cm}^{-1}\,\mathrm{sr}^{-1}$ for a fully protiated system (all systems have $n = 96.55\,\mathrm{atom\,nm}^{-3}$ at 298 K). Therefore it is clear that simple subtraction of a constant incoherent background does not account for the results (fig. 4.2).

At the position of the first structural peak and smaller-q range there exists a non-uniform increase of $\frac{d\Sigma}{d\Omega}$, with protiated dioxane, up to the equimolar fraction. This variation is the result of the combination of a coherent scattering change with molar fraction, and an incoherent background. With a fully protiated dioxane, the scattering intensity becomes dominated by the incoherent background and therefore featureless; except for the remaining broadened peaks (top curve, fig. 4.2). Therefore, we have identified the source of disagreement between experimental measurements and simulations as the degree of protiation of the sample, and we have also quantified the difference as a very sensitive function of the amounts of protiation. For instance, a 2 % mole fraction of $C_4H_8O_2$ can lead to $\approx 91\,\%$ higher scattering intensity in the small-q range (fig. 4.2).

To gain further insight into the discrepancies of measured and computed $\frac{d\Sigma}{d\Omega}$ we calculated its coherent part, first term on the right side of (4.1), as a function of the protiated dioxane molar fraction (figs. 4.3 and 4.4). Its variation increases with molar fraction up to equimolar (fig. 4.3), and decreases (to nearly zero) with molar fractions greater than 0.75 (fig. 4.4) for all values of q smaller than the first structural peak. Furthermore, there is relative less effect of the $C_4H_8O_2$ molar fraction on the coherent intensity in the q range greater than the structural peak position. In this range, it is noted a reverse variation with molar fraction, *i.e.* the intensity of scattering decreases up to equimolar molar fraction, then goes back again to almost initial levels with increasing molar fraction. Also, the second structural peak is lost with increasing molar fraction. These data (figs. 4.3 and 4.4) uncover the origin of the non-uniform variation of $\frac{d\Sigma}{d\Omega}$ with respect to hydrogen content (fig. 4.2) and shows that the coherent scattering intensity variation has a maximum around the equimolar fraction in the whole small-q range.

The behavior of the coherent part of (4.1) with varying protiation molar fraction (fig. 4.3 and 4.4) still remains to be understood. To that end, we looked at each con-

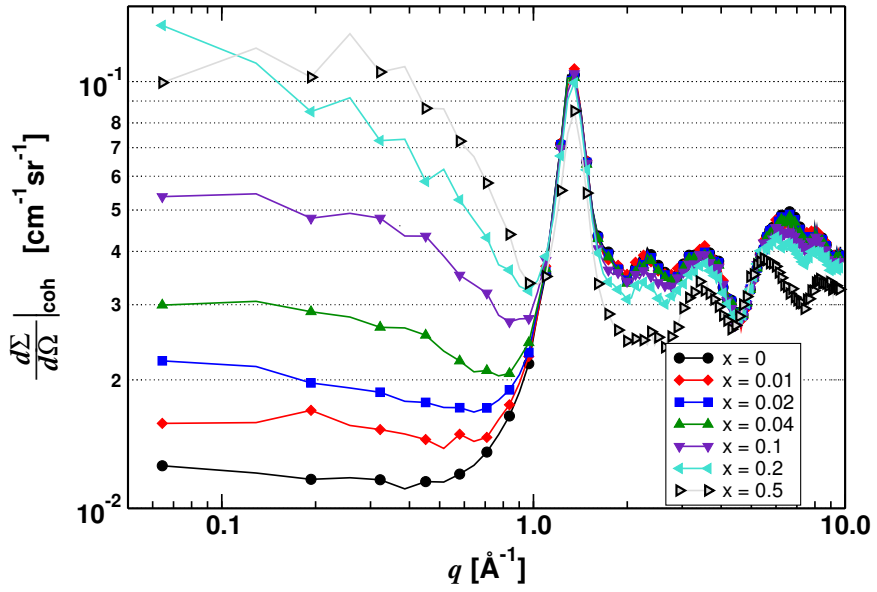

Fig. 4.3: *MD simulation of* $\left(\frac{d\Sigma}{d\Omega}\right)_{coh}$ *with increased levels of* $C_4H_8O_2$ *mole fractions (up to equimolar) of protiated dioxane at 298 K. Note coherent scattering affects the large-q intensity (after the first peak) by translating the curves vertically. An effect that is often attributed by authors to a flat incoherent background.*

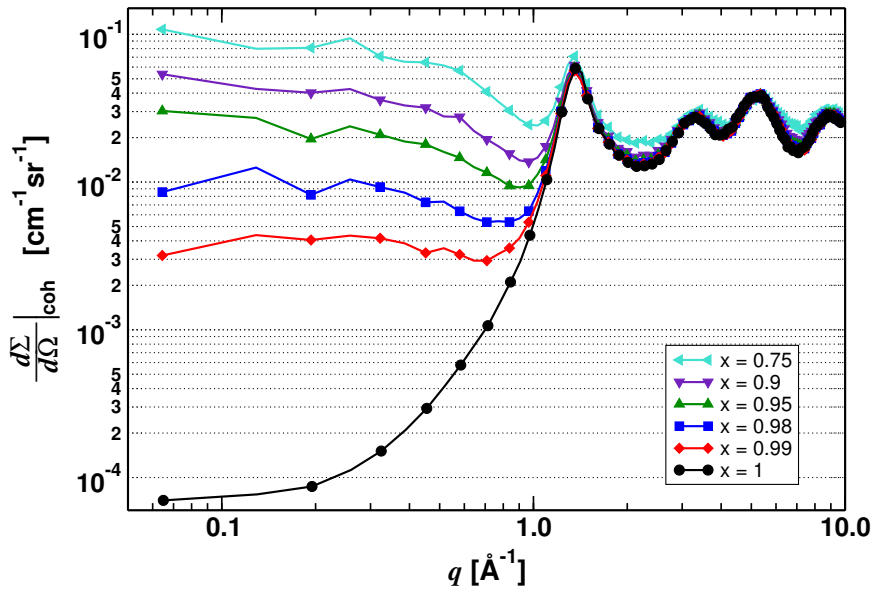

Fig. 4.4: *MD simulation of* $\left(\frac{d\Sigma}{d\Omega}\right)_{coh}$ *with increased levels of mole fractions (greater than equimolar) of protiated dioxane at 298 K.*

tribution of the weighed partial structure factors in the double sum of (4.1) (figs. 4.5, 4.6, 4.7, 4.8, 4.12, and 4.14). In the fully deuterated case, interference of all weighted structure factors is constructive for the small-q range (fig. 4.5, inset), and only three pairs contribute to destructive interference in the large-q range, namely OC, OD, and CD (note negative values in fig. 4.5). We established earlier that the first structural peak is of inter-molecular origin. Specifically, the weighted partial structure factors of the pairs CC, OC, CD are the main contributors to the formation of this peak. The second structural peak (intra-molecular origin) is the result of the constructive interference of the scattering of DD, CD, and CC pairs. While OD and OC contribute for the trough between the first and second peaks.

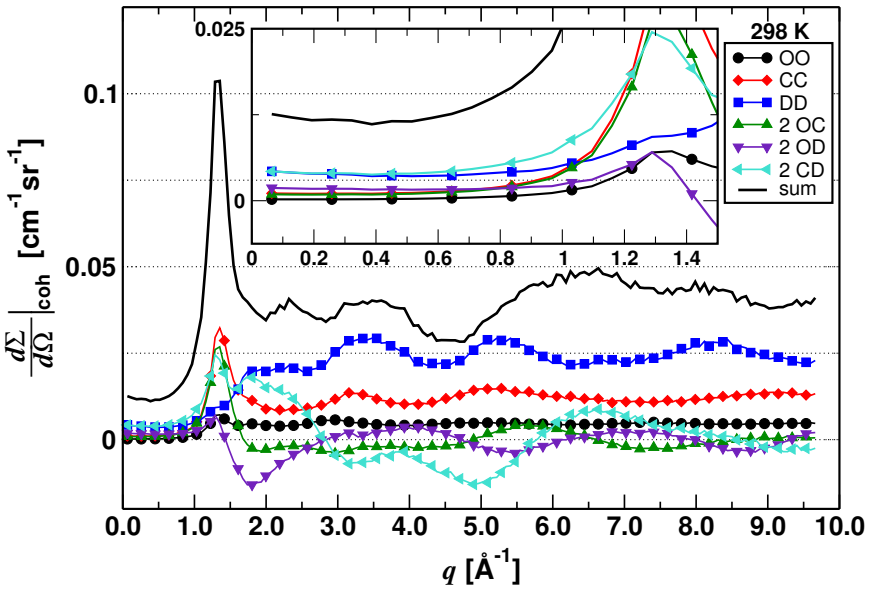

Fig. 4.5: *Computed (MD) weighted partial structure factors contribution,* $n\sqrt{w_\alpha\, w_\beta}\,\bar{b}_\alpha\bar{b}_\beta\, S_{\alpha\beta}(\boldsymbol{q})$*, for all 6 pairs of the fully deuterated system at 298 K.* DD > CD > OD *are the main contributors in the small-q range. The primary contributors to the first structural peak are* CC > OC > CD*. The large-q primary contributors are* DD > CC*.*

The introduction of protiated dioxane at 2 % prompts a net increase of scattering intensity at small q (note the "sum" curve above $0.0125\,\mathrm{cm}^{-1}\,\mathrm{sr}^{-1}$ in the inset of fig. 4.6) resulting from the new pair DH, and an increase in contribution from DD. The latter seems counter intuitive if the amount of D has decreased; this is related to a large length scale chemical inhomogeneity described later. As a reminder, the protiation scheme employed here is such that either a molecule is fully protiated or fully deuterated, therefore the DH contribution is only of inter-molecular origin.

With increased molar fraction of 10 %, additional net scattering intensity is predicted at small-q with dominant contribution from DD and twice DH (note "sum" curve above $0.025\,\mathrm{cm}^{-1}\,\mathrm{sr}^{-1}$ in the inset of fig. 4.7). Note that at large-q DD contributes significantly to the total scattering intensity while DH vanishes; the latter happens because the corresponding pair correlation is purely inter-molecular and it dies out very quickly with increasing q. There is virtually no reduction of the peak intensity, or any of the large-q structure. Note that a noticeable inter-molecular coherent scattering contribution at small-q from the HH pair also emerges and vanishes at larger q for the same reason as DH.

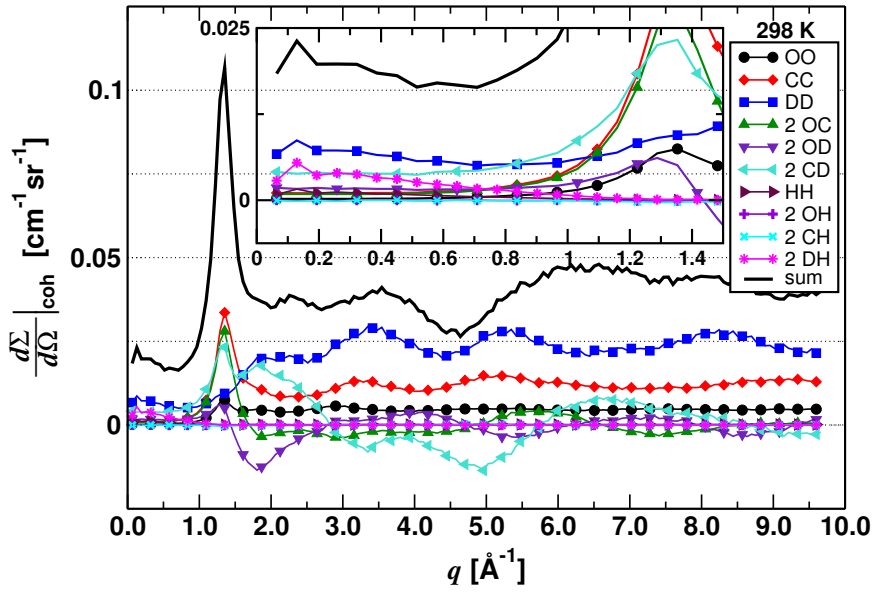

Fig. 4.6: *Computed (MD) weighted partial structure factors contribution for all 10 pairs at 2 % molar fraction protiation at 298 K.* DD > CD > DH *are the main contributors in the small-q range. All other contributors as in fig. 4.5.*

At equimolar fraction of protiated dioxane, the coherent scattering reaches its maximum in the small-q range and the contribution of the DD pair is primarily inter-molecular (fig. 4.8). Furthermore the contribution of DH equals that of DD, and HH also has a secondary role in contributing to an increase of coherent scattering in the small-q range. These results explain the increase of the contribution from the DD pair in the small-q range with reducing amounts of D. The contribution of DD increases due to inter-molecular coherent scattering, *i.e.*, with increased protiated fraction comes increased long wavelength chemical inhomogeneity. Here, at equimolar quantity, this inhomogeneity reaches its maximum. This is readily seen when comparing the partial structure factor S_{DD} at 0 %, 10 %, and 50 % protiation levels

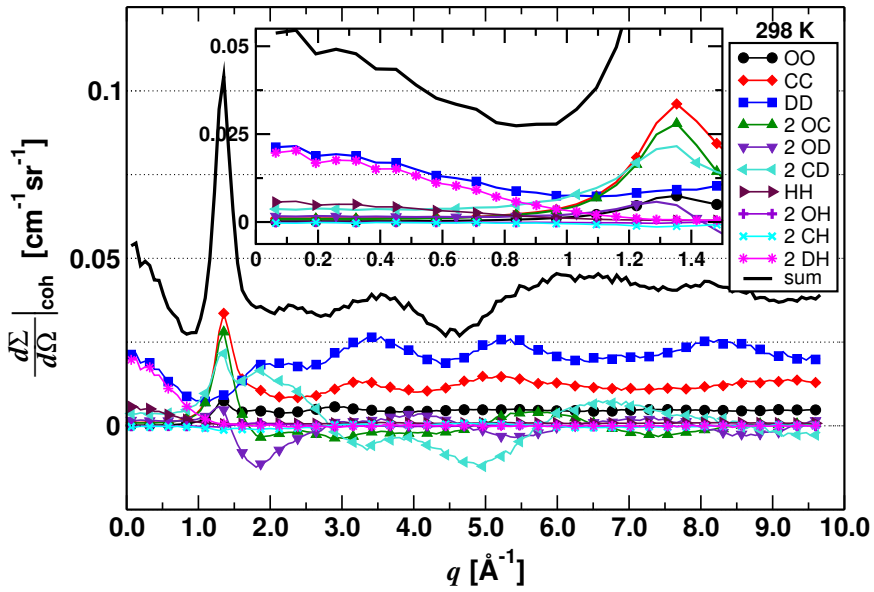

Fig. 4.7: *Computed (MD) weighted partial structure factors contribution for all 10 pairs at 10 % molar fraction protiation at 298 K.* DD > DH > HH *are the main contributors in the small-q range. The primary contributors to the larger-q range remain the same as with 2 % molar fraction (fig. 4.6).*

(figs. 4.9, 4.10, 4.11) and its coherent contribution, $n\, w_{\mathrm{D}}\, \overline{b}_{\mathrm{D}}^{2}\, S_{\mathrm{DD}}(\boldsymbol{q})$, to the differential scattering cross section. Still at equimolar fraction conditions, one observes that the small (negative) coherent scattering length of hydrogen reduces the intensity of all dissimilar pairs involving H in the large-q range (fig. 4.8).

We show results for 90 % molar fraction of protiated dioxane (fig. 4.12), for consistency, and demonstration that the contribution from the DH pair is the same as in the 10 % case (fig. 4.7), as it had to be since the scattering for the two cases have the same contrast. That is to say, the DH contribution, $n\sqrt{w_{\mathrm{D}}\, w_{\mathrm{H}}}\, \overline{b}_{\mathrm{D}} \overline{b}_{\mathrm{H}}\, S_{\mathrm{DH}}(\boldsymbol{q})$, is the same for 10 % or 90 % molar fractions since the product of the weights is the same, and $S_{\mathrm{DH}}(\boldsymbol{q})$ is also the same for all pairs of conjugated molar fractions (compare figs. 4.10 and 4.13); this is known as the Babinet's principle. The contribution of the CD pair causes destructive interference primarily under the first structural peak and therefore contributes significantly for the reduction of this peak height (fig. 4.12).

In the absence of deuteration, the anti-correlation of the CH and OH pairs balance the constructive interference of the remaining pairs to give an almost null coherent scattering intensity in the small-q range (fig. 4.14).

Equipped with unique insight provided by (MD) simulations, we carried out simulations with different amounts of protiated dioxane and found that 4 % molar fraction

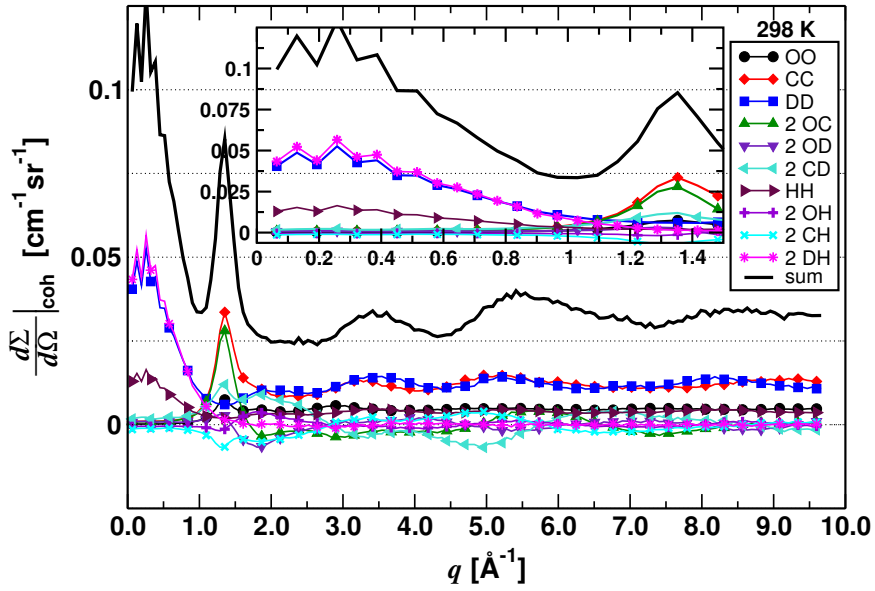

Fig. 4.8: *Computed (MD) weighted partial structure factors contribution for all 10 pairs at 50 % molar fraction protiation at 298 K.* DD ≈ DH *are the main contributors in the small-q range. The primary contributors to the larger-q range remain similar as with 10 % molar fraction (fig. 4.7) but now the CH pair has a noticeable destructive contribution under the first peak.*

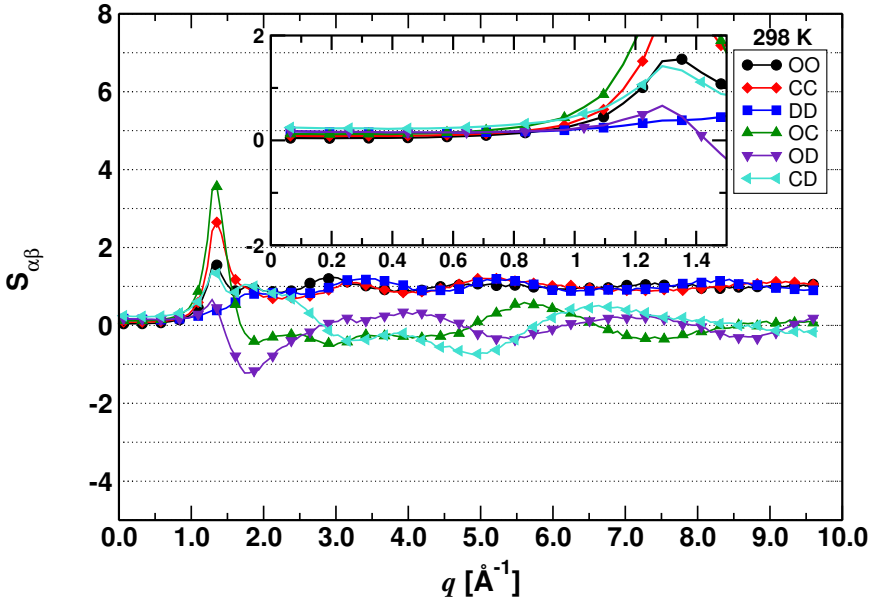

Fig. 4.9: *Computed (MD) true partial structure factors for either fully deuterated or fully protiated dioxane (replace D with H in the legend) at 298 K. Note* $\lim_{q\to\infty} S_{\alpha\beta} = \delta_{\alpha\beta}$.

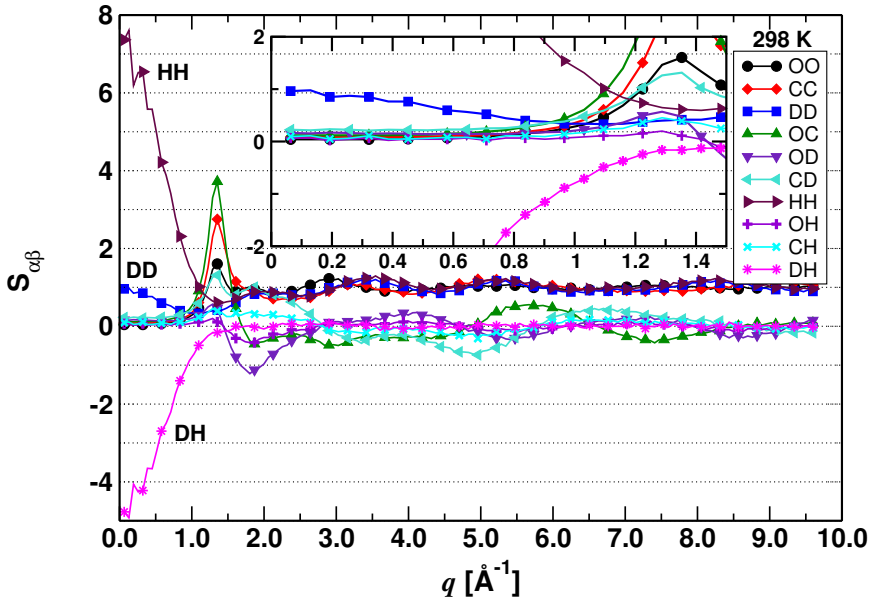

Fig. 4.10: *Computed (MD) true partial structure factors at 10 % molar fraction protiation at 298 K.*

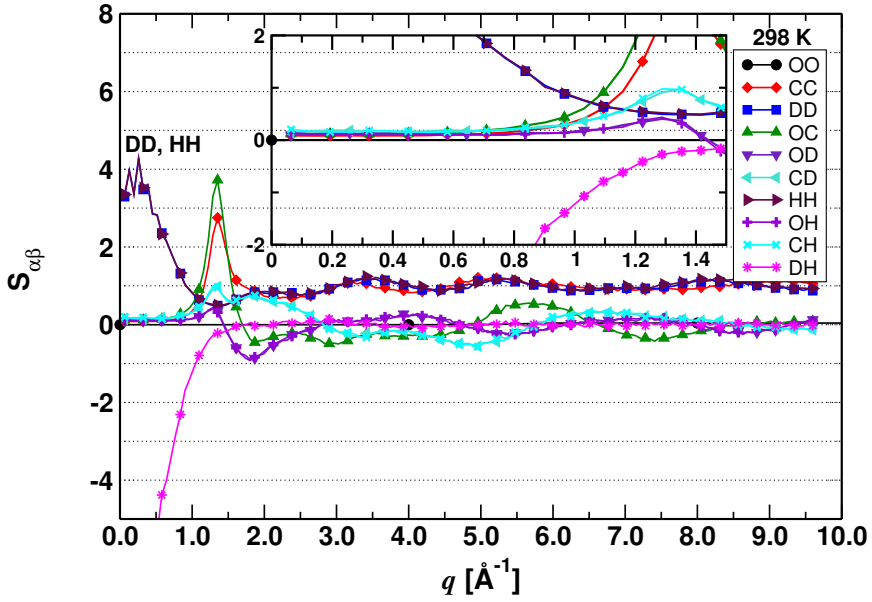

Fig. 4.11: *Computed (MD) true partial structure factors at 50 % molar fraction protiation at 298 K.*

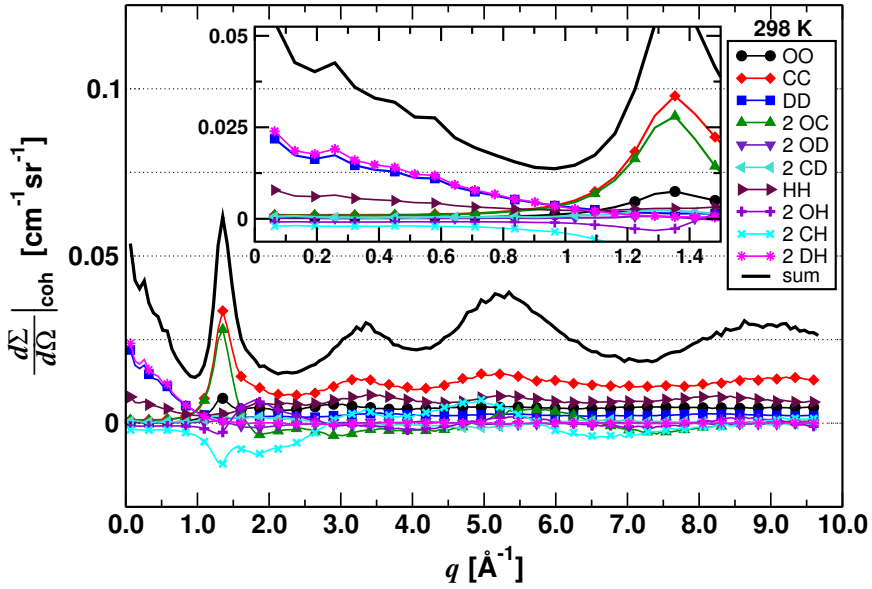

Fig. 4.12: *Computed (MD) weighted partial structure factors contribution for all 10 pairs at 90 % molar fraction protiation and 298 K.* DH ≈ CH *are the main contributors in the small-q range. The primary contributors to the larger-q range are* CC > DD. *Now CD produces a negative contribution under the primary peak.*

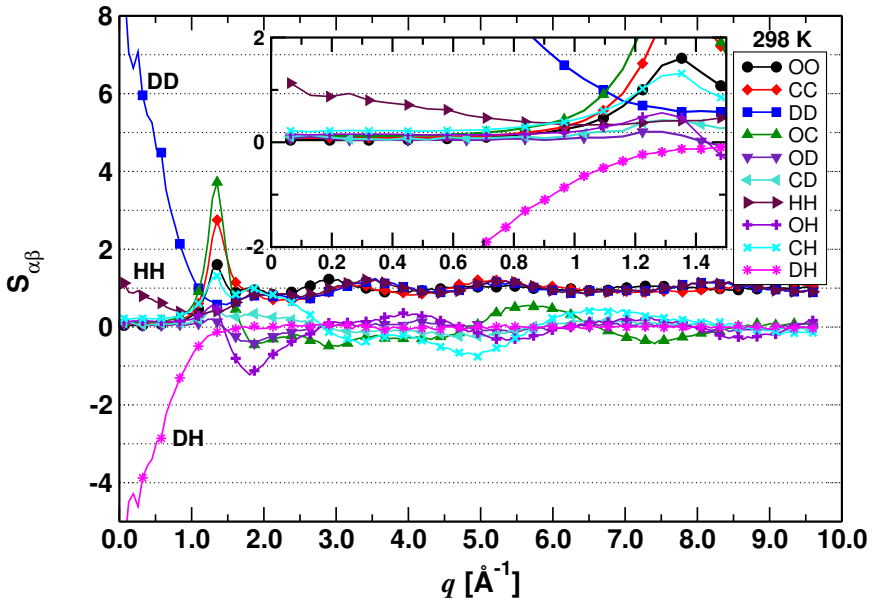

Fig. 4.13: *Computed (MD) true partial structure factors at 90 % molar fraction protiation at 298 K.*

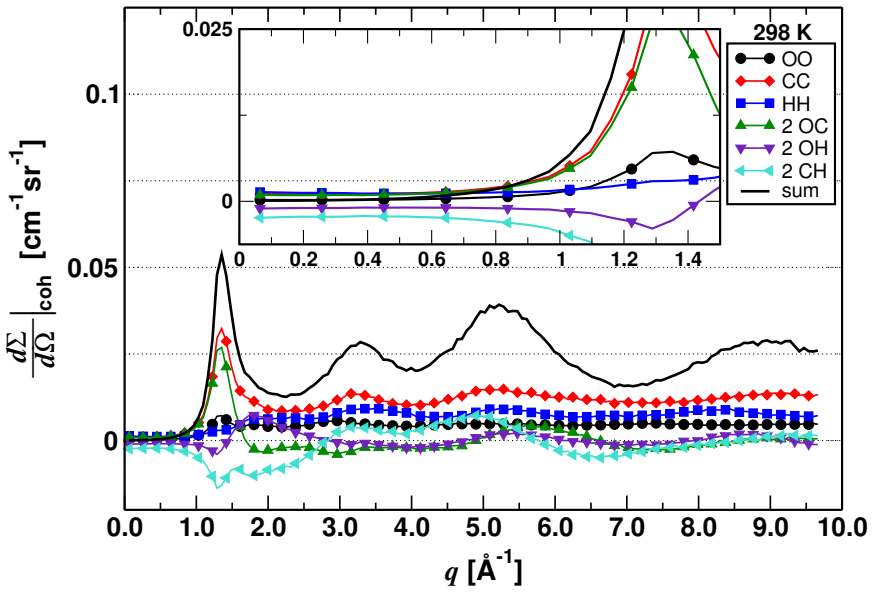

Fig. 4.14: *Computed (MD) weighted partial structure factors contribution for all 6 pairs of the fully protiated system at 298 K.* CC > OC *are the main contributors in the small-q range. The primary contributors to the larger-q range are* CC > HH *with a destructive contribution from CH and OH under the main peak.*

of $C_4H_8O_2$ in $C_4D_8O_2$ at 298 K produces results that match closely the SANS data, similarly, 5 % at 343 K (fig. 4.15) for the same sample. Furthermore, we found that

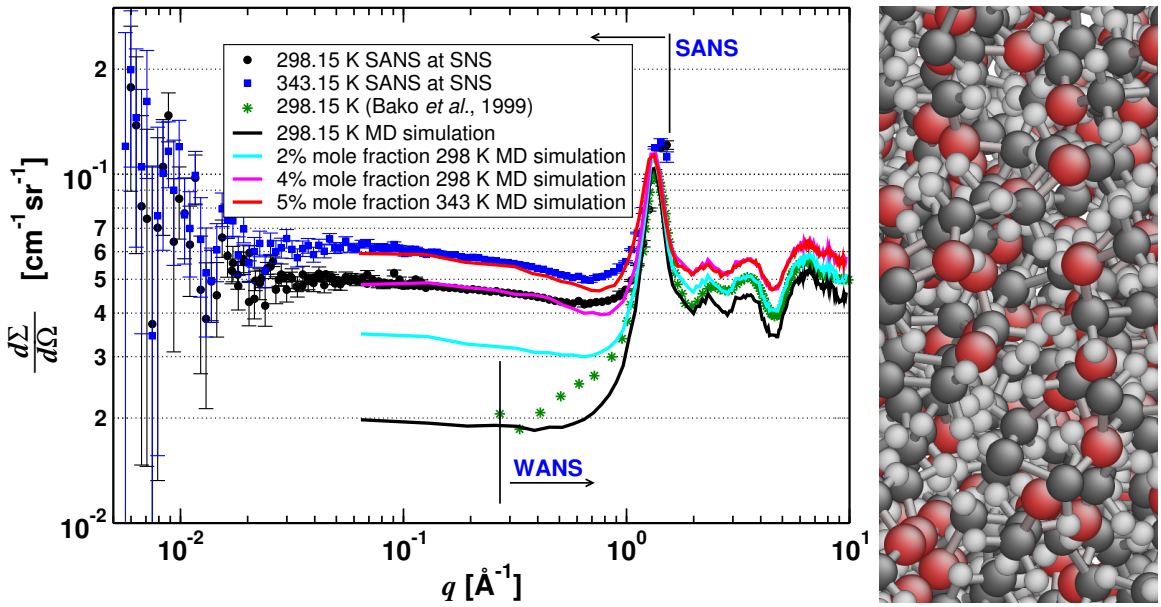

Fig. 4.15: *Left: Comparison of experimental data and MD simulation of the differential scattering cross section at two temperatures from a single sample. Right: snapshot of an MD simulation (red: oxygen atom, dark gray: carbon atom, light gray: deuterium atom).*

2 % molar fraction of $C_4H_8O_2$ in $C_4D_8O_2$ at 298 K matches the large-q range WANS data (fig. 4.15). Given the variability of the SANS experimental data (fig. 4.1) with respect to vendor and their quoted uncertainty on the percentage of deuteration (1 %), the MD simulation results are deemed in excellent agreement with experimental results (fig. 4.15); except in the heel region to the left of the first structural peak (to be discussed later).

Note we were able to reconcile simulation and experimental results by adding reasonable amounts of H to the simulated deuterated liquid at two different temperatures (fig. 4.15). The amounts of H needed for this outcome differ only by a few percent. Therefore we conjecture that in practice the percentage of deuteration quoted by vendors may be less than 99 % and/or additional controls are needed to produce higher quality deuterated samples in experiments.

In addition, we varied the scheme of protiation used from a) either a molecule is fully protiated or fully deuterated to b) random protiation of molecules. The results obtained differ significantly. That is, in b) almost all the coherence in the small-q range is destroyed. While in a) the results closely match the measured scattering

intensity. In view of these findings, we are led to speculate that the chemical deuteration process is likely to leave a molecule either fully deuterated or not deuterated at all.

We investigated the effect of temperature on the scattering intensity (fig. 4.16). In the small-q range scattering is increased while in the large-q range, the opposite

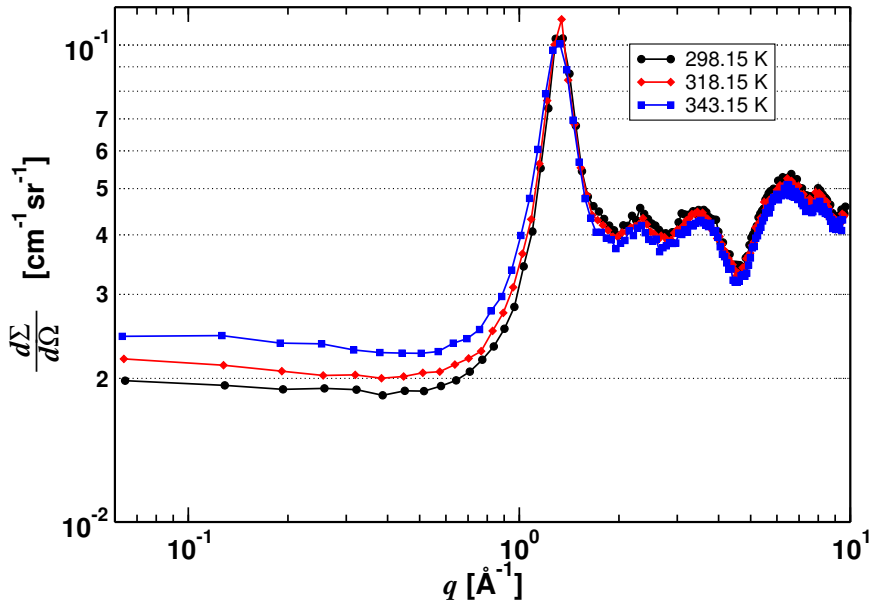

Fig. 4.16: *Variation of the MD simulated differential scattering cross section with temperature for fully deuterated 1,4-dioxane.*

occurs. In view of the decrease of the atom number density n with temperature (table 3.1) the behavior in the small-q range seems unexpected according to (2.10), which indicates the scattering intensity should decrease if the neutron total structure factor is not largely affected by temperature. However there is indeed a noticeable variation of $S_{\mathrm{n}}(\boldsymbol{q})$ in the small-q range as predicted by MD simulations (fig. 4.17) and the variation is sufficient to offset the decrease of n with temperature. Specifically, the weighted partial structure factors all increase with raising temperature in the small-q range, with the DD and CD pairs contributing the most (compare fig. 4.18 and 4.19). In this region, higher thermal fluctuation will increase the inhomogeneity of the sample and generate stronger interference of scattered neutrons. This is in accord with the reduction of the scattering intensity in the large-q range where thermal effects are less likely to affect the intra-molecular structure. Therefore the scattering intensity follows the reduction of the atomic number density n at large q.

We offer an explanation of the undershooting of the MD simulations at the heel region (fig. 4.15 and fig. 4.20), just before the first structural peak, based on inelastic

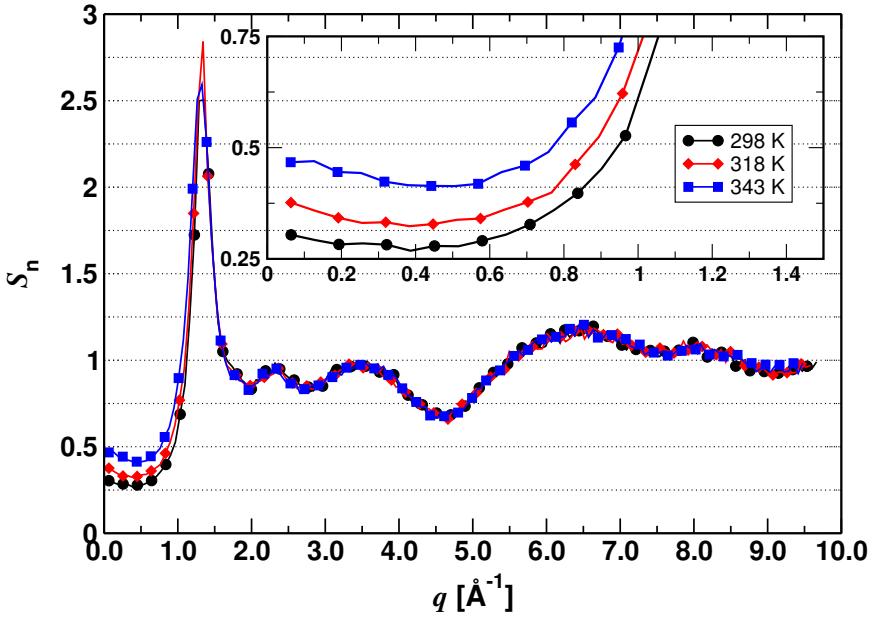

Fig. 4.17: *Variation of the MD simulated total neutron structure factor with temperature for fully deuterated dioxane.*

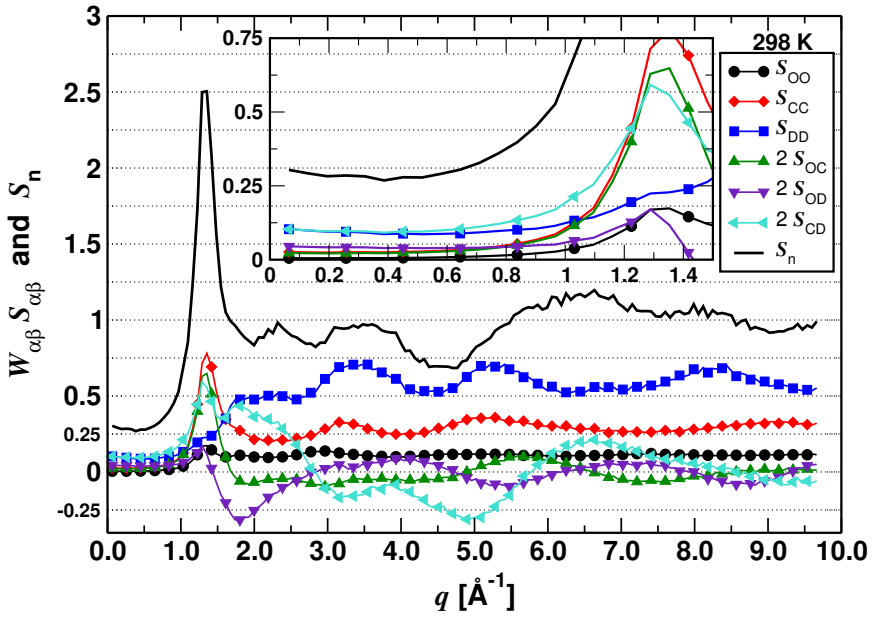

Fig. 4.18: *Computed (MD) fully deuterated weighted partial structure factors and the total neutron structure factor (sum of partial factors) at 298 K. The weights are* $\frac{4\pi}{\bar{\sigma}^{coh}}\sqrt{w_\alpha\, w_\beta}\,\bar{b}_\alpha\bar{b}_\beta$ (2.15b).

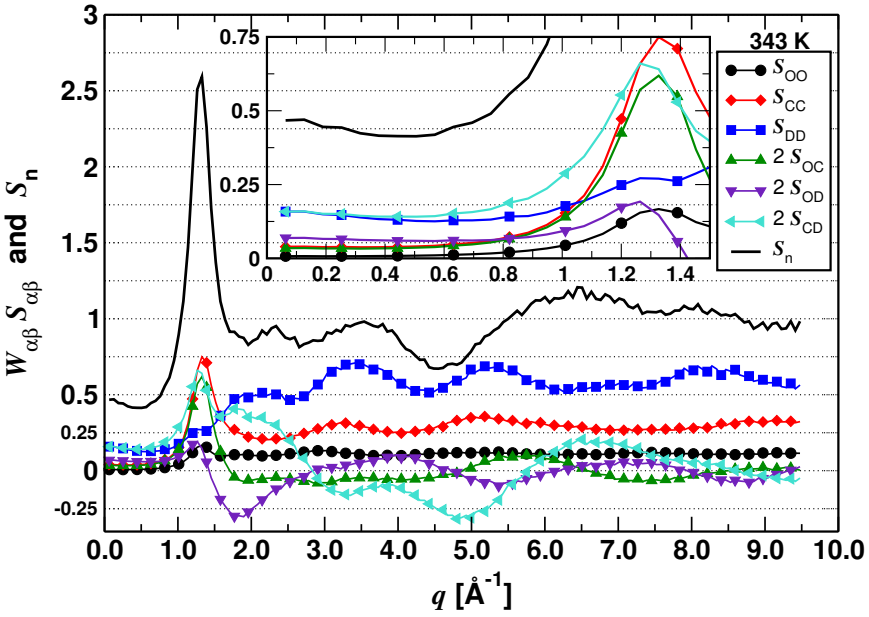

Fig. 4.19: *Computed (MD) fully deuterated weighted partial structure factors and the total neutron structure factor (sum of partial factors) at 343 K. The weights are* $\frac{4\pi}{\overline{\sigma}^{coh}}\sqrt{w_\alpha\, w_\beta}\,\overline{b}_\alpha\overline{b}_\beta$ (2.15b).

scattering effects present on instruments using the time-of-flight approach to determine the wavelength of a scattered neutron (Do *et al.*, 2014). Since the incoherent scattering cross section of hydrogen is large, an adverse effect can be noticed for low scattering liquids such as dioxane when even a small amount of hydrogen is present. For samples at elevated temperature there is a high probability for the neutron to gain energy when it scatters from hydrogen. These neutrons will arrive at the detector sooner than expected, overlapping in time with elastically scattered short-wavelength neutrons increasing their apparent count rate; thus increased measured intensity. Detailed modeling of this effect depends on the specifics of the molecular system under investigation and it is not a light undertaking. Instead, we advance the simple assumption that the effect is more likely to be caused by neutrons in the higher energy band used in our experiments, *i.e.*, 2 to 6.3 Å. Therefore, we can estimate the q-range where a conventional time-of-flight data reduction can be adversely affected by using the end points of the high-energy band, 2 Å and 6.3 Å, the distance from sample to detector, 1.3 m, and the detector size, 1 m × 1 m. Thus the maximum $q = \frac{4\pi}{\lambda}\sin\theta$ for each λ end point is obtained at maximum half scattering angle, $\approx 1/2\arctan(0.5/1.3) = 10.5°$, which leads to the estimated range $0.4\,\text{Å}^{-1} \leq q \leq 1.1\,\text{Å}^{-1}$. By subtracting the MD simulation results from the experimental SANS data (fig. 4.21) we find the difference

to be noticeable in the range $0.61\,\text{Å}^{-1} \leq q \leq 0.94\,\text{Å}^{-1}$ which is in good agreement with the estimated range of up-scattering effect. In addition, we observe the effect to be of the same magnitude (fig. 4.21) for both temperatures in the experiment. This is in agreement with the relatively short distance from the sample to the detector implying that up-scattering to an energy characteristic of either of the two sample temperatures will have approximately the same effect on the measured data; this further supports the foregoing conjecture.

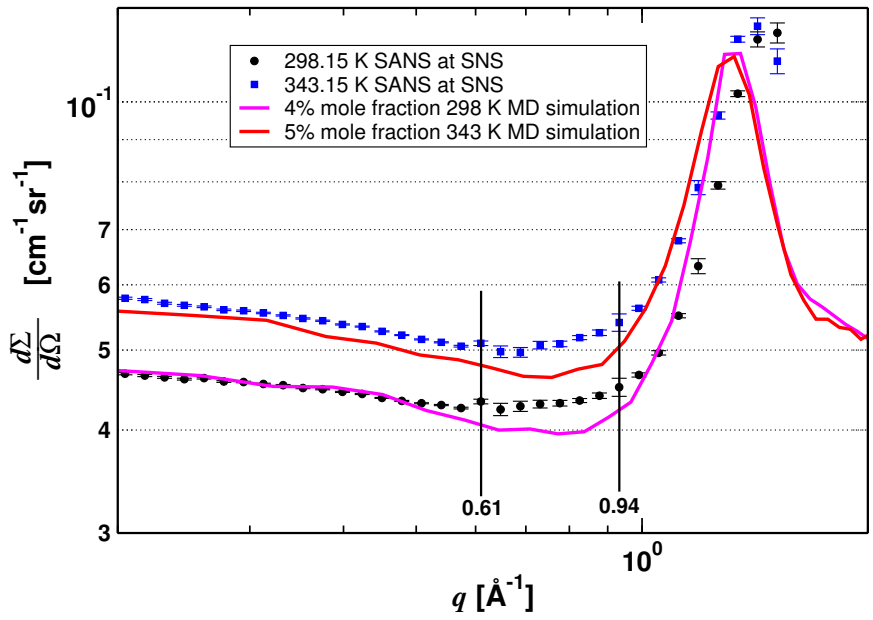

Fig. 4.20: *Zoom-in of the heel region to the left of the first structural peak (fig. 4.1). Comparison of experimental data and MD simulation of the differential scattering cross section.*

5 Conclusions

The original intent of this study was to validate the force field of classical molecular dynamics simulations applied to 1,4-dioxane liquid using static neutron scattering measurements (THOMAS *et al.*, 2007). This trend is becoming more attractive as scattering instruments become more sophisticated. Our comparison of experimental SANS and WANS data to computational results reveled disagreement in most of the q range measured; in particular, the small-q region (SANS). However after careful examination of the experimental data we found that the disagreement could be reconciled by performing simulations with higher levels of protiation than indicated by

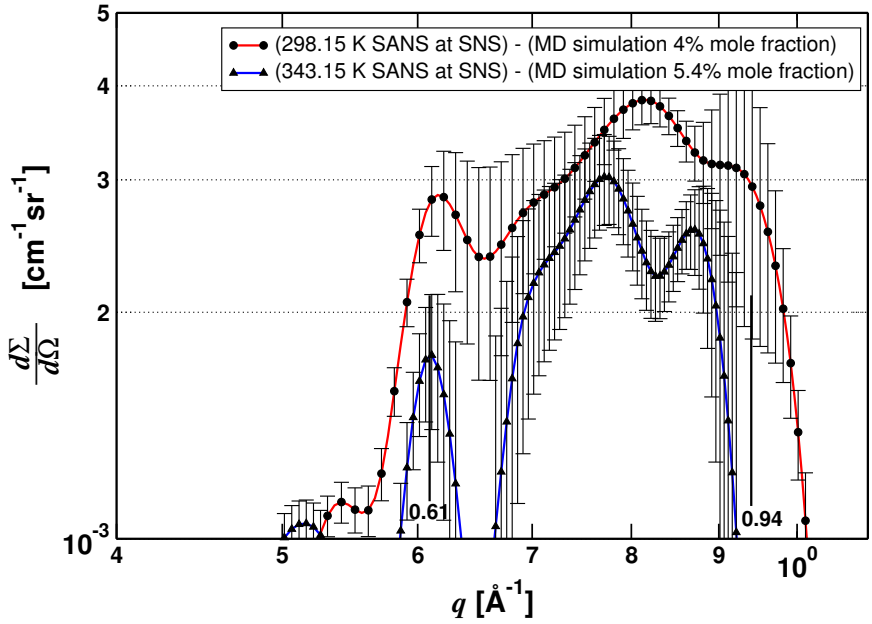

Fig. 4.21: *Difference between EQ-SANS scattering and MD simulations near the heel region (fig. 4.20). This represents an estimate of the inelastic scattering effect in the experimental data.*

the suppliers of 1,4-dioxane-d_8. Even small amounts of residual H affect substantially the small-angle scattering intensity because of the coherent scattering caused by the HD and DD atom pairs. We demonstrate this by extensive analysis of all computed partial structure factors as compared to the measured neutron total structure factor. The increased coherent scattering intensity obtained with additional residual H is a maximum at equimolar concentration and when the fluid is modeled as a mixture of molecules either fully deuterated or fully protiated.

In addition to the foregoing, instrument artifacts can create apparent disagreement between simulations and experimental data. In particular, instruments that rely on time-of-flight methods to determine neutron wavelength suffer from inelastic scattering events that change the neutron energy and thereby change the arrival time at the detector. We conjecture that this is the cause of the discrepancy in the heel region of our data. Although inelastic effects can be minimized in the data reduction, they cannot be fully eliminated, in particular for low scattering liquids (Soper, 2013).

Therefore what was initially an attempt to calibrate/validate a simulation method with experimental data, turned into understanding the experimental data using simulation results. This situation is likely to be found in similar studies and illustrates

that caution needs to be exercised in this particular area where scattering data is used to improve or validate molecular dynamics force fields (Houteghem *et al.*, 2014).

Acknowledgments

This work was partially supported by the Laboratory Director's Research and Development program of the Oak Ridge National Laboratory (ORNL) which is managed by UT-Battelle, LLC for the US Department of Energy (DOE) under contract No. DE-AC05-00OR22725. The research at the ORNL's Spallation Neutron Source was supported by the Scientific User Facilities Division through the Office of Basic Energy Sciences of DOE. The authors thank Dr. Changwoo Do, instrument scientist of the EQ-SANS diffractometer, for explaining the inelastic scattering effects on the data collected, and Dr. William T. Heller, lead instrument scientist, for discussions and help with absolute data calibration. Molecular dynamics simulations were performed at the Center for Advanced Modeling and Simulation of the Idaho National Laboratory, and at the DOE Office of Science Energy Research Scientific Computing Center.

References

Bako, I., Palinkas, G., Dore, J., and Fischer, H. **1999** Investigation of liquid 1,4-dioxane: an x-ray and neutron diffraction study. *Mol. Phys.* **96**(5) 743–47.

Benmore, C. J. and Loh, Y. L. **2000** The structure of liquid ethanol: A neutron diffraction and molecular dynamics study. *J. Chem. Phys.* **112**(13) 5877–5883.

Brocos, P., Calvo, E., Bravo, R., Pintos, M., Amigo, A., Roux, A. H., and Roux-Desgranges, G. **1999** Heat capacities, excess enthalpies, and volumes of mixtures containing cyclic ethers. 3. binary systems Tetrahydrofuran, Tetrahydropyran, 1,4-Dioxane, or 1,3-Dioxolane + Cyclohexane or Toluene. *Journal of Chemical Engineering Data* **44**(1) 67–72.

Cinacchi, G., Ingrosso, F., and Tani, A. **2006** Solvation dynamics by computer simulation: coumarin c153 in 1,4-dioxane. *J. Phys. Chem. B* **110**(27) 13633–41.

Contreras S, M. **2001** Densities and viscosities of binary mixtures of 1,4-dioxane with 1-propanol and 2-propanol at (25, 30, 35, and 40) °C. *Journal of Chemical Engineering Data* **46**(5) 1149–1152.

Do, C., Heller, W. T., Stanley, C., Gallmeier, F. X., Doucet, M., and Smith, G. S. **2014** Understanding inelastically scattered neutrons from water on a time-of-flight small-angle neutron scattering (sans) instrument. *Nucl. Instr. and Meth. A* **737** 42–6.

Geerlings, J. D., Varma, C. A. G. O., and van Hemert, M. C. **2000** Molecular dynamics studies of a dipole in liquid dioxanes. *J. Phy. Chem. B* **104**(1) 56–64.

Gray, C. G. and Gubbins, K. E. **1984** *Theory of Molecular Liquids: Fundamentals*, volume 1 of *The International Series of Monographs on Chemistry*. Clarendon Press, Oxford, Great Britain.

Gray, C. G., Gubbins, K. E., and Joslin, C. G. **2011** *Theory of Molecular Liquids: Applications*, volume 2 of *The International Series of Monographs on Chemistry*. Clarendon Press, Oxford, Great Britain.

Harrison, B. K. and Seaton, W. H. **1988** Solution to missing group problem for estimation of ideal gas heat capacities. *Industrial Engineering Chemistry Research* **27**(8) 1536–1540.

Holz, M., Heil, S. R., and Sacco, A. **2000** Temperature-dependent self-diffusion coefficients of water and six selected molecular liquids for calibration in accurate 1h nmr pfg measurements. *Phys. Chem. Chem. Phys.* **2** 4740–4742.

Houteghem, M. V., Ghysels, A., Verstraelem, T., Poelmans, W., and Waroquier, M. **2014** Critical analysis of the accuracy of models predicting or extracting liquid structure information. *J. Phys. Chem. B* **118**(118) 2451–70.

Humphrey, W., Dalke, A., and Schulten, K. **1996** Visual molecular dynamics. *J. Mol. Graphics Modell.* **14** 33–8.

Krienke, H., Ahn-Ercan, G., and Barthel, J. **2004** Alkali metal halide solutions in 1,4-dioxanewater mixtures. a monte carlo simulation study. *J. Mol. Liq.* **109**(2) 115 – 124.

Liu, H. and Maginn, E. **2011** A molecular dynamics investigation of the structural and dynamic properties of the ionic liquid 1-n-butyl-3-methyl imidazolium bis(trifluoromethanesulfonyl)imide. *The Journal of Chemical Physics* **135**(12) 124507.

Lovesey, S. W. **1984** *Theory of Neutron Scattering from Condensed Matter: Nuclear Scattering*, volume 1 of *The International Series of Monographs on Physics*. Clarendon Press, Oxford, Great Britain.

Martínez, L., Andrade, R., Birgin, E. G., and Martínez, J. M. **2009** Packmol: A package for building initial configurations for molecular dynamics simulations. *J. Comp. Chem.* **30**(13) 2157–2164.

Nagy, P. I., Völgyi, G., and Takács-Novák, K. **2008** Monte carlo structure simulations for aqueous 1,4-dioxane solutions. *J. Phys. Chem. B* **112**(7) 2085–2094. PMID: 18220380.

Plimpton, S. **1995** Fast parallel algorithms for short-range molecular dynamics. *J. Comput. Phys.* **117** 1–19. http://lammps.sandia.gov.

Soper, A. K. **2013** The radial distribution function of water as derived from radiation total scattering experiments: Is there anything we can say for sure? *ISRN Phys. Chem.* **2013**(279463) 1–67.

Squires, G. L. **1996** *Introduction to the Theory of Thermal Neutron Scattering*. Dover Publications, Inc., New York, New York. Originally published in 1978 by Cambridge University Press.

Thomas, J. L., Tobias, D. J., and MacKerell Jr., A. D. **2007** Direct comparisons of experimental and calculated neutron structure factors of pure solvents as a method for force field validation. *J. Phys. Chem. B Lett.* **111** 12941–4.

Villares, A., Martin, S., Haro, M., Giner, B., and Artigas, H. **2004** Densities and speeds of sound for binary mixtures (1,3-dioxolane or 1,4-dioxane) with (2-methyl-1-propanol or 2-methyl-2-propanol) at the temperatures (298.15 and 313.15) K. *J. Chem. Thermodyn.* **36** 1027–36.

Zhao, J. **2000** Extended q-range, high intensity, high precision small angle diffractometer. Technical Document IS-1.1.8.2-6036-RE-A-00, SNS 107080100-TD0001-R00, Spallation Neutron Source, Oak Ridge National Laboratory, Oak Ridge, TN 37831, U.S.A.

Zhao, J. **2001** Supplement to extended q-range, high intensity, high precision small angle diffractometer. Technical Document SNS 107080100-TD0002-R00, Spallation Neutron Source, Oak Ridge National Laboratory, Oak Ridge, TN 37831, U.S.A.

Zhao, J. K., Gao, C. Y., and Liu, D. **2010** The extended q-range small-angle neutron scattering diffractometer at the sns. *J. Appl. Cryst.* **43** 1068–77.